



---

Unterschrift Betreuer

# Diplomarbeit

## Simulation and Design of a Z-Field Sensitive Spin Polarized GMR Sensor

zur Erlangung des akademischen Grades

**Diplom-Ingenieur**

im Rahmen des Master Studiums

**Technische Physik**

eingereicht von

**Benedikt Holzmann**

Matrikelnummer 00725863

Ausgeführt am Institut für Festkörperphysik  
an der Fakultät für Physik der Technischen Universität Wien

unter der Anleitung von  
Privatdoz. Dipl.-Ing. Dr.techn. Dieter Suess  
Dipl.-Phys. Dr. Claas Abert

## Zusammenfassung

Magnetfeldsensoren sind in vielen unterschiedlichen Ausführungen und Anwendungen zu finden. Sie werden zum Beispiel zur Drehzahlmessung in Autos oder auch einfach zum Auslesen von Daten auf Magnetstreifen, wie einer Kreditkarte, eingesetzt. Um Daten auslesen zu können, ist es notwendig zwischen zwei binären Zuständen unterscheiden zu können. In Strukturen, welche aus wenige nm dünnen, übereinander gestapelten Schichten aus Ferromagneten und Nichtmagneten aufgebaut sind, ist der Riesenmagnetowiderstand (GMR) der maßgeblich verantwortliche Effekt der Widerstandsänderung.

Ziel der vorliegenden Arbeit ist es, ein neues Sensorkonzept zu entwickeln, welches auf dem Spin-Transfer-Torque beruht und es erlaubt, die Stärke und Richtung einer einzelnen Komponente eines Magnetfeldes, der  $z$ -Komponente, zu bestimmen. Dabei werden neben dem Riesenmagnetowiderstand noch der Übertrag eines Drehmoments durch spinpolarisierte Elektronen (Spin-Torque) auf die magnetische Struktur des Sensors und eine intrinsische Eigenschaft der verwendeten Materialien, die es ihnen erlaubt, ihre Magnetisierung senkrecht zu ihrer Oberfläche auszurichten (PMA), ausgenutzt.

Im Folgenden werden die, dem Sensor zugrundeliegenden Konzepte diskutiert und seine Funktionsweise vorgestellt. Danach folgt eine Einführung in die theoretischen Konzepte, die zur Beschreibung des Sensors notwendig sind. Im Anschluss daran werden erste Simulationen des vorgeschlagenen Sensordesigns durchgeführt, um seine Funktionsfähigkeit zu zeigen und die Kenngrößen Sensitivität  $S$  und Detektivität  $D$  zu bestimmen.

## Abstract

Magnetic field sensors exist in many different designs, meant for many different applications. For example, they are used in cars to measure the rotational speed of wheels or simply read data from magnetic strips of e.g. credit cards. In order to be able to read data, it is necessary to distinguish between two binary states. In structures made of multiple, several nm thin ferromagnetic and nonmagnetic layers, the main effect responsible for a change of resistance is called giant magnetoresistance (GMR).

The aim of the thesis at hand is to develop a new sensor concept based upon spin-transfer-torque, that not only distinguishes between two field directions, but also is sensitive to the strength of one single field component, the z-component. Beside the giant magnetoresistance, the spin-torque, which is exerted by spin polarized electrons acting on the magnetic configuration of the sensor, and an intrinsic property of the used materials, the perpendicular magnetic anisotropy (PMA), are crucial to make the sensor design viable.

Following, the underlying concepts of the proposed sensor design and its principle of operation will be discussed. This is concluded with an introduction to the theoretical concepts required to properly describe the sensor. Finally, initial simulations of the proposed sensor design will be conducted in order to demonstrate its viability and determine the parameters sensitivity  $S$  and detectivity  $D$ .

## Danksagung

An dieser Stelle möchte ich mich bei meinem Betreuer, Privatdoz. Dipl.-Ing. Dr.techn. Dieter Suess, bedanken, der meine Diplomarbeit erst ermöglicht hat. Für seine Geduld und seine Expertise, mit der er mir oftmals entscheidend weiterhelfen konnte, möchte ich mich besonders bedanken. Auch schätze ich es sehr, dass er mich während meiner Arbeit finanziell unterstützt hat.

Ein ganz besonderer Dank gilt auch meinem Zweitbetreuer, Dipl.-Phys. Dr. Claas Abert. In intensiven Diskussionen fand er stets die nötige Zeit, um gemeinsam an Problemlösungen zu arbeiten und mir einen tieferen Einblick in die Thematik zu vermitteln. Auch ihm möchte ich daher ausdrücklich für seine Geduld und motivierenden Worte danken, sollte es einmal nicht ganz so gut gelaufen sein, wie gewollt.

Nicht unerwähnt soll die gesamte Arbeitsgruppe bleiben, in der ich immer ein offenes Ohr und eine helfende Hand fand. Die großartige Atmosphäre innerhalb der Gruppe trug maßgeblich zur Freude an der Arbeit bei - Vielen Dank!

Abschließend möchte ich meiner Freundin, meinen Freunden und meiner Familie meinen unermesslichen Dank aussprechen, dafür, dass sie meine Klagen genauso ertragen haben, wie meine endlosen Vorträge über kleinere und größere Erfolgserlebnisse. Ganz besonders und ausdrücklich möchte ich mich bei meinen Eltern, Andrea und Rudolf, bedanken, die mir mit ihrer finanziellen Unterstützung ein Studium ermöglicht haben und es immer geschafft haben, mir den nötigen Rückhalt und Schubs in die richtige Richtung zu geben.

# Contents

<b>1</b>	<b>Introduction</b>	<b>6</b>
<b>2</b>	<b>Z-Field Sensitive Sensor</b>	<b>7</b>
2.1	GMR - Giant Magnetoresistance . . . . .	7
2.2	In-Plane vs. Perpendicular to Plane GMR Sensors . . . . .	7
2.3	Hysteresis of a Perpendicular Magnetic Anisotropy Ferromagnet . . . . .	10
2.4	Spin-Torque . . . . .	12
2.5	Principle of Operation . . . . .	15
2.6	Sensitivity and Detectivity . . . . .	17
2.7	Sensor Structure and Specifics . . . . .	18
<b>3</b>	<b>Micromagnetic Theory</b>	<b>20</b>
3.1	Landau-Lifshitz Equation . . . . .	20
3.2	Landau-Lifshitz-Gilbert Equation . . . . .	23
3.3	The Effective Field $\mathbf{H}_{\text{eff}}$ . . . . .	24
3.4	Anisotropy-Field Energy . . . . .	24
3.5	Exchange-Field Energy . . . . .	28
3.6	Stray-Field Energy . . . . .	29
3.7	Zeeman-Field Energy . . . . .	30
3.8	Stochastic Landau-Lifshitz-Gilbert Equation . . . . .	30
3.9	The Spin-Diffusion Model . . . . .	31
3.10	Energy Barrier and Thermal Stability . . . . .	32
<b>4</b>	<b>Numerical Simulations</b>	<b>35</b>
4.1	Deterministic Simulations with Simplified Model . . . . .	35
4.1.1	Single Free Layer . . . . .	35
4.1.2	Additional Soft Magnetic Layer . . . . .	38
4.2	Stochastic Simulations . . . . .	45
<b>5</b>	<b>Conclusion</b>	<b>50</b>

# 1 Introduction

The intention of the presented sensor design is to measure the z-field component  $H_{\text{ext}}$  of an external magnetic field  $\mathbf{H} = \{H_x, H_y, H_{\text{ext}}\}^T$  via a change of the sensor's resistance, compare Fig. 1. When an applied electric current density  $\mathbf{j}_e = \{0, 0, j\}^T$  reaches a critical value, the so-called switching current  $j_s$ , the magnetic configuration of the sensor changes from one of the two possible states to the other. While an antiparallel state ( $\uparrow\downarrow$  or  $\downarrow\uparrow$ ) results in a higher electric resistance, a parallel state ( $\uparrow\uparrow$  or  $\downarrow\downarrow$ ) yields a lower resistance state. This is the principle of any GMR device, compare Sec. 2.2. In order to achieve magnetic reversal in the sensor, the concept of spin-torque, see Sec. 2.4, is employed, which leads to asymmetric switching currents  $|j_s^{\uparrow\downarrow\leftarrow\uparrow\uparrow}| \neq |j_s^{\uparrow\uparrow\leftarrow\uparrow\downarrow}|$ , see Sec. 2.3. Assuming an external magnetic field  $H_{\text{ext}} \neq 0$ , it has a de-/stabilizing effect on the sensor's magnetic configuration and thus shifts the switching currents distinctively, allowing conclusions on the field strength. Being exclusively sensitive to the z-component of a magnetic field is made possible by the use of ferromagnetic metals with an uniaxial perpendicular magnetic anisotropy axis, that is assumed to be collinear with the z-field component. Hence, when combined with an GMR sensor that is sensible to the planar components of an external field, the proposed z-field sensor allows to draw information from all three vector components.

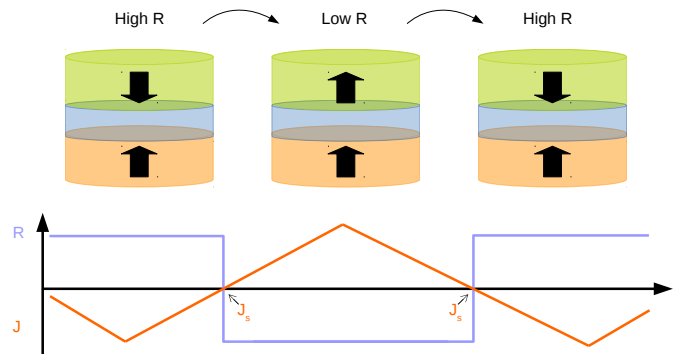


Figure 1: Schematic of the sensor's working principle. Switching between high/low/high/low... resistance states results in a characteristic resistance over time curve. Switching occurs at a critical current, the switching current  $j_s$ .

## 2 Z-Field Sensitive Sensor

### 2.1 GMR - Giant Magnetoresistance

The basic concept on which the sensor of investigation is based upon, is called giant magnetoresistance (GMR). It is a quantum mechanical effect that appears in thin-film multilayer structures of alternating ferromagnetic and nonmagnetic, conductive layers and was initially described in experiments published by Baibich et al. [1] and Binasch et al. [2]. The effect describes the change of electrical resistance due to a change in the magnetic alignment of the different ferromagnetic layers within the examined system, based on spin dependent conductivity, which shows a particularly strong change at interfaces between nonmagnetic and magnetic layers [3]. The general expression to describe the change of magnetoresistance reads as follows

$$\text{MR} = \frac{R(0) - R(H)}{R(0)} \quad , \quad (2.1)$$

where MR is the fraction of the difference of resistance at zero magnetic field  $R(0)$  and  $R(H)$ , the resistance at a magnetic field value of  $H$ , divided by the resistance at zero field strength. Achievable values of MR (here GMR) were reported at a magnitude of several percent at room temperature [4] and about 50% at a temperature of  $T = 4.2\text{ K}$  [1]. For the purpose of the proposed sensor a slightly different definition of magnetoresistance is more appropriate

$$\text{MR} = \frac{R_{ap} - R_p}{R_p} \quad , \quad (2.2)$$

where  $R_{ap}$  and  $R_p$  denote the resistance values for the antiparallel and parallel state, respectively, with  $R_{ap} > R_p$ .

### 2.2 In-Plane vs. Perpendicular to Plane GMR Sensors

A basic GMR sensor consists of two thin, ferromagnetic alloys, sandwiching another thin, nonmagnetic spacer layer. A sketch of said device, showing its high and low resistance state, is given in Fig. 2. In case of a vanishing external magnetic field (left schematic), electrons entering the system (yellow arrow) with an antiparallel configuration of magnetizations (antiparallel, black arrows in ferromagnetic layers) are subject to strong scattering, indicating a state of higher resistance. The right schematic depicts the low-resistance state, in which due to an external magnetic field, a parallel magnetization configuration is achieved and electrons can pass more easily. Due to the ferromagnets'

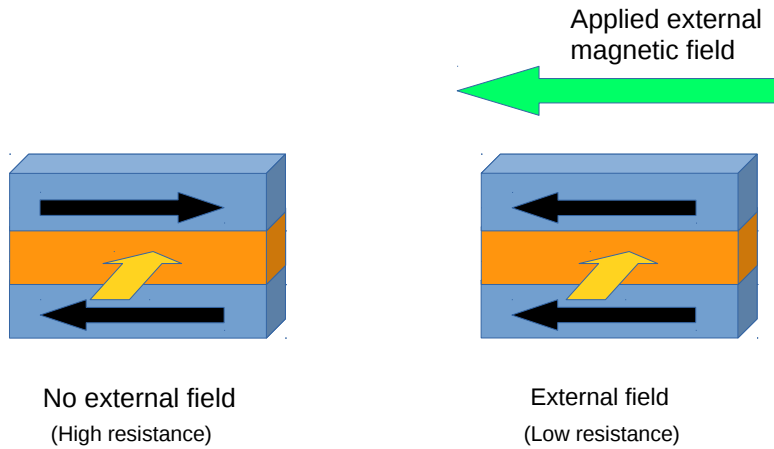


Figure 2: Schematic of a basic GMR sensor in high-resistance state (left) with antiparallel magnetizations (black arrows) and in low-resistance state (right) with parallel aligned magnetizations. A change between high and low resistance is achieved via application of an external magnetic field (green arrow). Electrons passing the sensor are indicated by yellow arrows.

design, their magnetizations can only rotate in-plane and therefore are only sensitive to the planar components of the external field. For an existing angle between the external field and the sensor's plane, the magnetization simply does not rotate into saturation, leading to a magnetic state that is neither fully parallel nor completely antiparallel. This means, that the current flowing through the sensor stack is subject to a certain resistance, depending on the magnetization state in that direction, which is a measure for the external field's component in that direction.

In order to obtain higher GMR values for the proposed sensor design, the current perpendicular to plain (CPP) geometry is used. In contrast to a current in-plane (CIP) setup, as it is often used for GMR devices, the current has to pass each layer of the sensor consecutively when using the CPP configuration, see Fig. 3, thus leading to higher GMR values. Furthermore, the CPP geometry is the imperative feature that makes spin-torque, see Sec. 2.4, accessible.

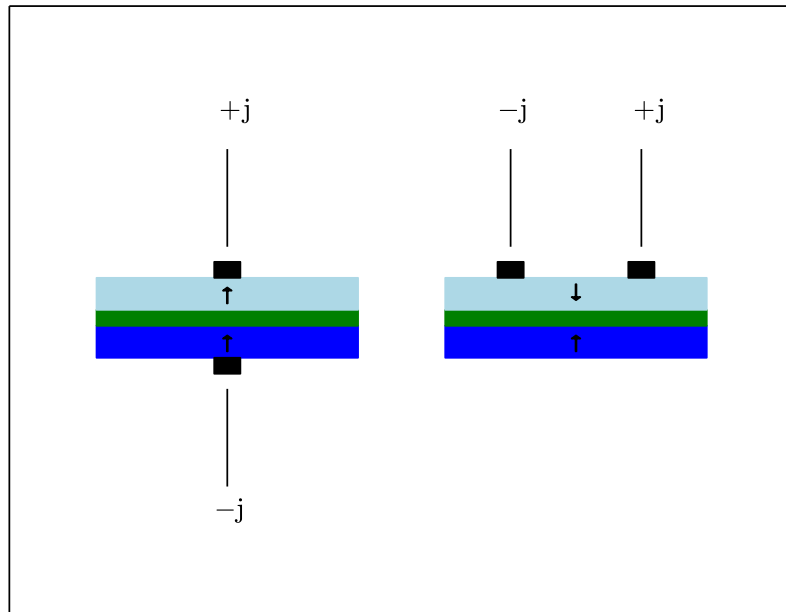


Figure 3: Basic structure of a GMR stack with different wiring. On top of the bottom ferromagnetic layer (fixed layer), there is the paramagnetic spacer layer, on top of which the top ferromagnetic layer (free layer) is attached. Black arrows indicate possible magnetization configurations: parallel (left) and antiparallel (right). Only the left stack will be used for the proposed z-field sensor, since it features the current perpendicular to plane (CPP) configuration, where the current flows through each layer consecutively, opposed to the current in-plane (CIP) configuration for the right stack, where both electrical contacts are on top of the free layer.

### 2.3 Hysteresis of a Perpendicular Magnetic Anisotropy Ferromagnet

As discussed in the previous subsection, the sensor employs a CPP configuration, such that the surface normal of the sensor is parallel to the z-axis. In order to be sensitive to magnetic fields along that particular direction, the ferromagnetic alloys are manufactured with a perpendicular magnetic anisotropy (PMA) axis, that also lies parallel to the z-axis or easy axis, see Fig. 9. Ferromagnetic materials, such as these, exhibit an important property known as magnetic hysteresis, that is crucial for the operation of the proposed sensor.

Figure 4 shows two hysteresis curves of the same hard magnetic layer but for two different heights. These curves show some of the main characteristics of a hard magnetic material that are important to operate the sensor. Firstly, it can be seen that for the most part, the magnetization, which is normalized to the saturation magnetization  $M_s$ , occupies one of the two possible extremal states at  $m_z = \pm 1$ . Secondly, the transition between those states happens at a quick rate which results in a steep slope. Thirdly, the roots of these curves, which are defined as 'switching-current densities'  $j_s$  throughout this thesis, appear at large values of the applied current density  $j$ .

It should be noted, that in general the graph of a magnetic hysteresis loop is a plot of magnetization over the applied field. The proposed sensor though, aims to relate the switching-current densities to the applied field and therefore the hysteresis representation of the magnetization plotted over the current density is more appropriate, while both representations include the same information.

At this point the comparison with an ideal hard magnetic layer shall be made. Its hysteresis curve takes the shape of a perfect rectangle. Thus it can be said, that for the case of a perfect hard magnet, the entirety of its magnetization occupies one of the two states  $m_z = \pm 1$  at any given point in time, since the switch from  $m_z = +1$  to  $m_z = -1$  and vice versa happens instantaneously at  $j_s$ .

The rounded corners, which appear in both depicted curves in Fig. 4, are the result of a small angle between the anisotropy axis of the magnetic layer and the applied field. This angle is introduced into the system in order to allow the start of magnetization reversal processes even for small perturbations, i.e. small magnetic fields. The transition from one state to the other does not happen instantly but instead takes place over a short range of the current density  $\Delta j$  around  $j_s$ . However, the fact that the switching process happens within a small region  $|\Delta j| \ll |j_s|$  means, that the magnetization still can be treated as existing in one single state for the most part. Additionally, values for  $|j_s|$  in a hard magnetic layer are higher compared to those in a soft magnetic layer, which lead

to a bigger area enclosed by the hysteresis curve. Since a larger area demands higher energy consumption in order to achieve magnetic reversal, a large area, i.e. large values of  $|j_s|$  together with a constant magnetization of  $m_z = \pm 1$ , can be treated as an indicator for a higher stability of the magnetic configuration. The two shown curves in Fig. 4 feature an asymmetry in their respective switching-current densities with  $|-j_s| \neq |j_s|$ , originating in the combination of a spin-torque, see Sec. 2.4, that introduces an inherent asymmetry to the current hysteresis loops, and an external field  $H_{\text{ext}}$ , that shifts the loops sideways. This relative shift, caused by the magnetic field, allows conclusions not

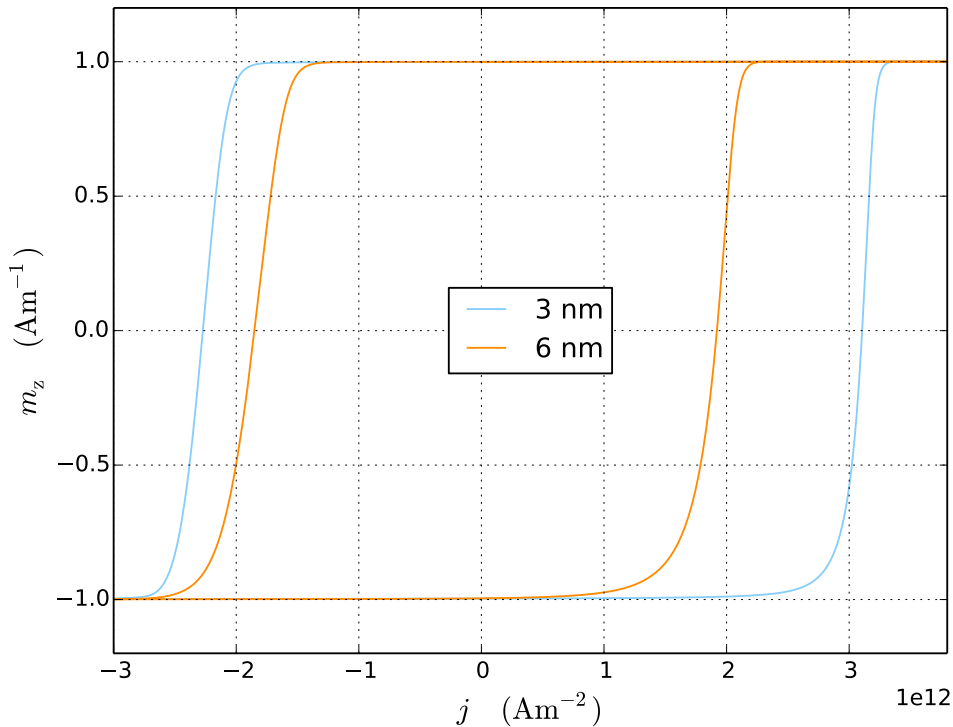


Figure 4: Hysteresis curves of a hard magnetic layer of 3 nm and 6 nm height under the influence of spin-torque and a magnetic field  $H_{\text{ext}}$ . In comparison to the hysteresis curve of an ideal hard magnetic layer (symmetric rectangle centered at the origin), which is not shown here, the depicted curves feature an asymmetry in their roots, with respect to the origin, as well as rounded corners due to a small angle between the anisotropy axis of the ferromagnetic layers and the applied magnetic field.

only on the direction of  $H_{\text{ext}}$ , but also on its actual strength, see discussion in Sec. 2.5.

## 2.4 Spin-Torque

In the previous section the appearance of an asymmetry of the ferromagnet's hysteresis curve has been discussed and its origin has been claimed to lie in the existence of a spin-torque. For the purpose of the thesis at hand, a basic understanding and description of this phenomenon will be sufficient and therefore more interested readers are referred to e.g. a paper of Slonczewski [5] in which a framework of electron transport through a thin spacer layer, sandwiched by two ferromagnetic layers, is presented.

The presented sensor exhibits the design of a typical device exploiting spin-torque. It consists of two ferromagnetic, metallic layers, that sandwich a nonmagnetic spacer layer and two nonmagnetic leads that enclose this trilayer, see Fig. 5. If an electric current is applied to such a multilayer stack, the conducting electrons are affected by spin dependent scattering processes. These result in a spin polarization of the conducting electrons, i. e. an electric current that can be assumed to have an equally distributed spin population among the conducting electrons when entering the device, will develop a shift in its spin distribution, so that a majority-spin and a minority-spin class exist throughout the multilayer. Especially interfaces between magnetic and nonmagnetic layers can be considered as the main scattering sites, since the difference in local magnetizations at these interfaces changes rapidly. Figure 5 gives a schematic representation of spin dependent scattering processes for a parallel (right) and antiparallel (left) magnetization configuration of the sensor.

Considering an unpolarized current, represented by the black arrow passing through the center of the multilayer, with its equally distributed spin populations, expressed by leftward pointing orange arrows and rightward pointing green arrows along the current line, the first scattering site is the interface between L1 (nonmagnetic lead) and FM1 (first ferromagnetic layer). Although there will be back scattered electrons in L1, carrying the same spin as the magnetization of FM1 (large orange arrow), only such electrons with opposing spin are depicted (small orange and green arrows off the current line), since they make up the majority of the scattered electrons. Due to this scattering process, the electric current is considered to be spin polarized, since it now carries a majority spin according to the magnetization configuration of FM1. For a sufficiently thin nonmagnetic spacer layer NM, this polarization is carried to the next scattering site, the interface between NM and FM2 (second ferromagnetic layer). This time two phenomena occur. On the one hand, the polarized current exerts a torque, the spin-torque, on the magnetization of FM2 (large green arrow) and, if strong enough, induces magnetic reversal, if the starting configuration of FM1 and FM2 is antiparallel. On the other hand, since

the current's majority spin opposes the magnetization of FM2, electrons of that spin population are reflected and have a stabilizing effect on the magnetization of FM1. Considering a parallel configuration of FM1's and FM2's magnetization, facts are exchanged at the interface between NM and FM2. Due to the magnetization configuration in FM2 showing the same alignment as the majority spin of the electrical current, a stabilization of FM2's magnetization is achieved. At the same time, back scattered electrons exert a torque on the magnetization of FM1 and can induce a switching process in this layer.

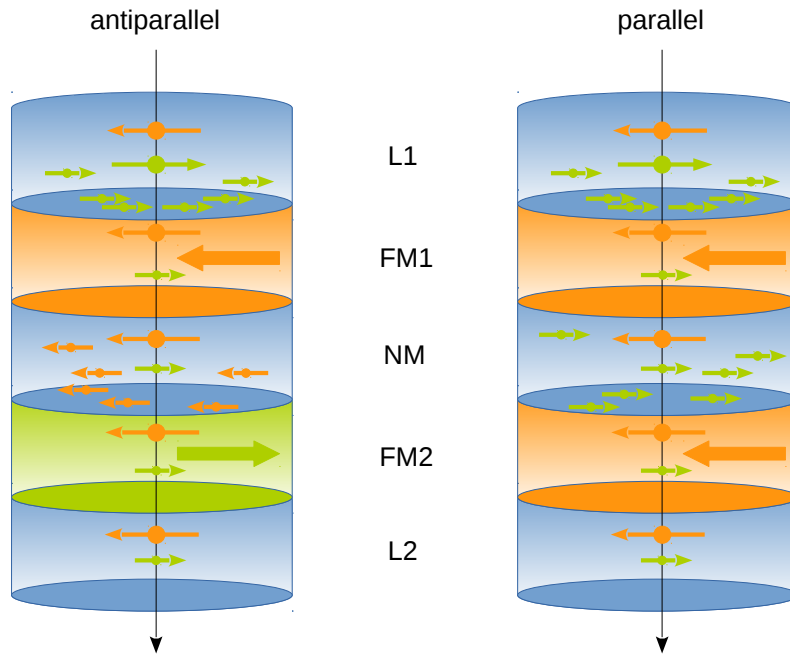


Figure 5: Schematic of the spin dependent scattering process in a multilayer with magnetic layers FM1, FM2 and nonmagnetic layers L1, L2 and NM. For both cases, the parallel as well as the antiparallel configuration of FM1 and FM2, the interface L1/FM1 acts as a spin polarizing site. The polarized current then exerts a spin-torque in FM2, while back scattered electrons show a stabilizing effect in FM1 for an antiparallel starting configuration of FM1 and FM2. In case of a parallel magnetization configuration, the spin-torque is exerted by the back scattered electrons in FM1, while stabilization occurs in FM2.

## 2.5 Principle of Operation

In order to get a working sensor, the three discussed ingredients plus the external field

- Perpendicular Magnetic Anisotropy (PMA)
- GMR
- Spin-Torque
- $H_{\text{ext}}$

have to be combined into one collaborating system. While the intrinsic PMA of the ferromagnetic layers accounts for the sensibility along a distinct direction (z-axis), the applied current has to perform two tasks. First, it has to induce the switching process between the antiparallel and parallel state (spin-torque) and secondly, it has to supply the sensor readout signal (GMR). Employing Fig.6, the principle of the sensor's signal generation shall be discussed. The top left corner shows two hysteresis loops, tilted by  $90^\circ$ , such that the  $j$ -axis matches the  $j$ -axis of the top right plot. This diagram shows the evolution of the sensor's driving current  $j$  over time  $t$ . Without loss of generality, the driving current is assumed to be a symmetric and periodic function of time. Thus, it can be written as a combination of just odd harmonics of the fundamental and is assumed to have the form

$$j(t) = \sum_{i=0}^N j_{(2i+1)} \sin [(2i + 1)\omega t] \quad , \quad (2.3)$$

where  $j(t)$  is the time dependent current along the z-axis,  $\omega = 2\pi\nu$  is the angular frequency and  $2i + 1$  denotes the mode number. In the case shown in Fig. 6, the driving current is represented by a triangular wave, matching the just mentioned conditions of  $j(t)$ .

Starting in the top left corner and following the dashed, horizontal lines to the right, intersections of these lines with the driving current can be found. These intersections mark the switching currents  $j_s^+$  and  $j_s^-$ , at which the magnetization configuration jumps from one state to the other. By following the vertical dashed lines towards the bottom plot, the influence of  $j_s^+$  and  $j_s^-$  on the shape of the output signal can be seen. By plotting the magnetization  $M$ , which is related to the sensor's resistance over time  $t$ , a rectangular function is deduced from the triangular driving function. The green diagram cycle shows the signal creation of a perfectly square hysteresis curve, which

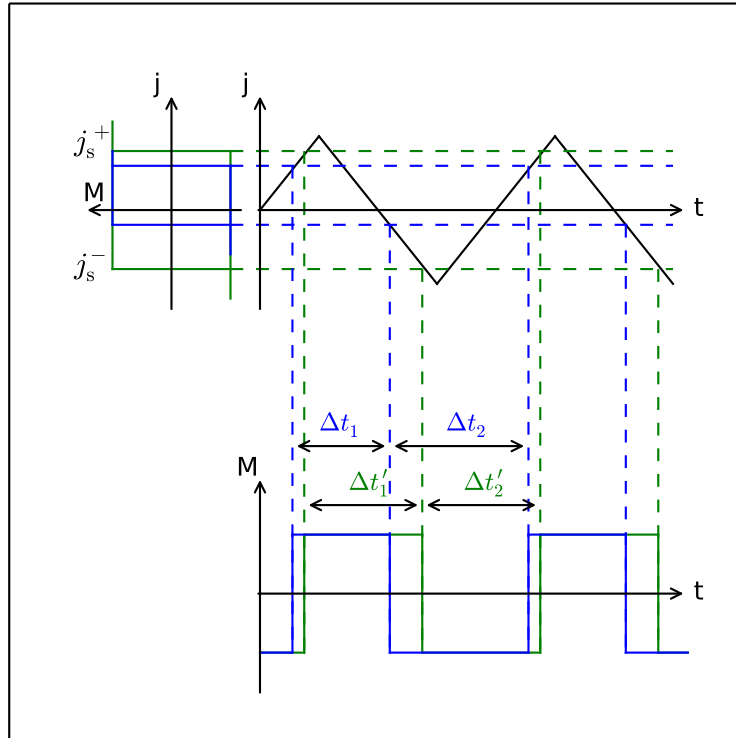


Figure 6: Generation of a rectangular output signal with a triangular driving current density  $j$ .  $M$  denotes the magnetization and  $t$  the time. Green symbols are related to the unperturbed square signal ( $\Delta t'_1 = \Delta t'_2$ ) of an ideal ferromagnet with a symmetric hysteresis curve, whereas blue symbols denote the asymmetric shift ( $\Delta t_1 \neq \Delta t_2$ ) evoked by the spin-torque and an external field  $H_{\text{ext}} \neq 0$ . Switching currents are indicated by  $j_s^+$  and  $j_s^-$ .

would resemble a perfectly square output signal. The blue cycle on the other hand depicts the case of a hysteresis that is under the effect of spin-torque and an external field  $H_{\text{ext}} \neq 0$  and thus shows an asymmetry in the switching currents, leading to a rectangular output signal with  $\Delta t_1 \neq \Delta t_2$ .

As described in e.g. [6], a Fourier transformation of a square output signal and of a driving signal like the one given in (2.3), both consist of just odd harmonics. Through the introduction of an asymmetry (spin-torque) to the hysteresis, a change from the square output function into a rectangular one is achieved and even harmonics appear in the frequency spectrum. If the sensor is further affected by an external magnetic field  $H_{\text{ext}} \neq 0$ , its hysteresis curve will be subject to yet another source of asymmetry. Hence, analysis of the even harmonics, especially the 2<sup>nd</sup>, as its magnitude is larger than the magnitude of higher order ones, allow conclusions on the magnitude of the external field.

## 2.6 Sensitivity and Detectivity

There are two main quantities of interest when a sensor is to be characterised. The first one is called sensor sensitivity or sensor gain  $S$ .  $S$  sets the measured magnetic field  $H$  and the output signal of the sensor, the current density  $j_{\text{out}}$ , in correlation. For an ideal sensor, the transfer characteristic is linear, and can thus be written as simple as

$$j_{\text{out}} = S \cdot H \quad . \quad (2.4)$$

The second quantity is the so called detectivity  $D$ . It is related to the minimum detectable field of a sensor, and thus limits the sensor's resolution.  $D$  is fundamentally coupled to intrinsic noise and is therefore often mathematically described with the help of the power spectral density (PSD) of noise or rather the spectral density  $S(\nu)$  of noise, since the noise depends on the frequency range  $\Delta\nu$  [7].  $D$  can be written as

$$D = \frac{1}{\sqrt{2}} B_0 \sqrt{t} \quad \text{with dimension} \quad [D] = \text{T}/\sqrt{\text{Hz}}, \quad (2.5)$$

where  $B_0$  means the magnetic field and  $t$  is the measurement time. This minimum detectable field  $B_0$  certainly depends on the standard deviation  $\sigma_{\mu_0 H}$  of the measured data. In case of the stochastic simulations, that are presented in Sec. 4.2, the standard deviation  $\sigma_j$  has the dimension of a current density, since the measure of interest is the switching-current density  $j_s$ . Thus, following Eq. (2.4), the sensor's sensitivity  $S = \partial j / \partial \mu_0 H$  is used to calculate the field uncertainty  $\sigma_{\mu_0 H}$

$$\sigma_{\mu_0 H} = \frac{1}{S} \sigma_j = \frac{\partial \mu_0 H}{\partial j} \sigma_j \quad \text{with dimension} \quad [\sigma_{\mu_0 H}] = \text{T} \quad , \quad (2.6)$$

which then can be inserted into equation (2.5). Hence, the detectivity can be written as

$$\begin{aligned} D &= \frac{1}{\sqrt{2}} \cdot \sigma_{\mu_0 H} \cdot \sqrt{t} = \frac{1}{\sqrt{2}} \cdot \frac{1}{S} \cdot \sigma_j \cdot \sqrt{t} \\ &= \frac{1}{\sqrt{2}} \cdot \frac{\partial \mu_0 H}{\partial j} \cdot \sigma_j \cdot \sqrt{t} \quad , \end{aligned} \quad (2.7)$$

where  $\mu_0 = 1.256\,637\,061\,4 \times 10^{-6} \text{ N A}^{-2}$  is the magnetic field constant and  $H$  is the external field, given in  $\text{A m}^{-1}$ . From this equation it can be seen, that by increasing the measurement time by e.g. a factor of  $10^6$ , the minimum detectable field can be reduced by a factor of  $1/\sqrt{10^6} = 10^{-3}$ .

## 2.7 Sensor Structure and Specifics

In this section the proposed design of the multilayer stack will be introduced and explained and the specifics of each thin-film will be given.

In Fig. 7 the complete multilayer structure of the proposed sensor is depicted. The

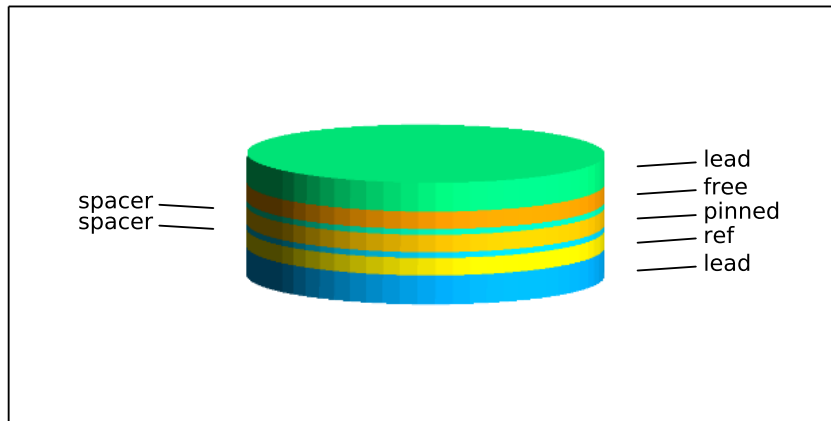


Figure 7: The sensor's complete multilayer structure. Ferromagnetic layers are named free, pinned and reference (ref). The lead and spacer layers are nonmagnetic, conducting layers.

sensor is supposed to be operated in a current perpendicular to plane mode. This forces the current density  $j_e$  to pass through every single layer in succession, thus leading to a stronger change of resistance, see Section 2.2. The top and bottom layers are the two leads that provide the current to the sensor. Each of them is modelled to simulate a conducting, but nonmagnetic material. On top of the bottom lead, there is the first ferromagnetic layer, that is called reference layer throughout this thesis. It, as well, is electrically conducting, but exhibits magnetic characteristics of a ferromagnetic transition d-metal. This layer is followed by the first spacer layer, separating the reference layer from the next ferromagnetic layer, the pinned layer. Beside the task of building a separation between two ferromagnetic regions, the spacer also has to be electrically

conducting and it must be able to facilitate magnetic exchange coupling between the reference and the pinned layer. The latter lies beneath another spacer layer and exhibits equal magnetic and electric features as the reference layer. The second spacer, which is modelled to have the same properties as the prior mentioned spacer, has one important difference. Exchange coupling between the pinned and the free layer is reduced, compared to the coupling of the reference and the pinned layer, in order to loosen the rigid magnetic system, acting on the free layer's magnetization. Arriving at the upper end of the stack, only the last ferromagnetic layer, the free layer, is left to mention. It as well, is a conductor and shows magnetic behaviour of a ferromagnetic transition metal. Each layer has a radius  $r = 30$  nm but differs in height, i.e. elongation along the z-axis, which is assumed to be parallel to the uniaxial symmetry axis of the sensor. From bottom to top, the thin-films have heights of  $d_z = 5$  nm, 3 nm, 1 nm, 3 nm, 1 nm, 3 nm and 5 nm. The ferromagnetic layers exhibit a common saturation magnetization of  $M_s = 7.1 \times 10^5$  A m<sup>-1</sup> and uniaxial anisotropy constants of  $K_{\text{uni}} = 1 \times 10^6$  J/m<sup>3</sup>,  $1 \times 10^6$  J/m<sup>3</sup> and  $2 \times 10^5$  J/m<sup>3</sup> for the reference-, pinned- and free layer, respectively. It is common to treat the combination of the reference-, spacer- and pinned layer as one single ferromagnetic layer, which then is called the fixed layer. This pattern of how to construct the fixed layer is introduced, in order to stabilize the pinned layer via an antiferromagnetic coupling to the reference layer, i.e. stabilize its magnetization and thus make it more resilient to magnetic reversal processes. Due to the artificial character of such a trilayer, it is also called synthetic antiferromagnet (SAF), compare e.g. [8].

### 3 Micromagnetic Theory

According to [9], micromagnetics deals with the determination of hysteresis loops from local quantities. Modern micromagnetism though often deals with magnetic features on length scales between 1 nm and 1  $\mu$ m. The description of such phenomena has started with the introduction of a classic continuum theory by Landau and Lifshitz [10]. This theory works if the following conditions are met. First, the magnetic moments  $\mathbf{m}$  of neighbouring atoms at positions  $\mathbf{r}_i, \mathbf{r}_j$  are assumed to point in approximately the same direction

$$\mathbf{m}(\mathbf{r}_i) \approx \mathbf{m}(\mathbf{r}_j) \quad . \quad (3.1)$$

Second, the discrete magnetic moments  $\mathbf{m}_i$ , with  $i \in \{1, \dots, N\}$ , where  $N$  is the total number of atoms throughout the ferromagnetic sample, are considered to be homogeneously distributed. These two conditions allow for the total magnetization  $\mathbf{M}(\mathbf{r}_i)$  to be approximated as a continuous vector field

$$\mathbf{M}(\mathbf{r}_i) \rightarrow \mathbf{M}(\mathbf{r}) \quad (3.2)$$

and the total magnetization  $\mathbf{M}(\mathbf{r})$  can be considered to have a constant magnitude of  $M_s$ , the ferromagnet's saturation magnetization or spontaneous magnetization

$$|\mathbf{M}(\mathbf{r})| = M_s \quad , \quad (3.3)$$

so that only the direction between  $\mathbf{M}(\mathbf{r})$  and  $\mathbf{M}(\mathbf{r} + \Delta\mathbf{r})$  may vary throughout the ferromagnet.

#### 3.1 Landau-Lifshitz Equation

In the following, a brief proof of the valid classical treatment of the purely quantum mechanical subject, electron spin dynamics, will be given. For simplicity a single spin  $\mathbf{s}$  in an external magnetic field  $\mathbf{H}$  is the object under investigation. The Zeeman Hamiltonian for this system thus reads

$$\hat{\mathcal{H}} = \frac{g_e \mu_0 \mu_B}{\hbar} \mathbf{H} \hat{\mathbf{S}} \quad . \quad (3.4)$$

Here  $g_e = 2$ ,  $\mu_0$ ,  $\mu_B$  and  $\hbar$  are the Landé g-factor of the electron, the magnetic field constant or vacuum permeability, the Bohr magneton and the reduced Planck constant, respectively and  $\mathbf{H}$  is the external magnetic field. The vector  $\hat{\mathbf{S}}$  is formed by the  $2 \times 2$

Pauli matrices, which are the elemental objects of the spin operator [11]

$$\hat{\mathbf{S}} = \frac{1}{2}\hbar\hat{\boldsymbol{\sigma}} \quad . \quad (3.5)$$

In a next step, the quantum mechanical expectation value of the spin operator  $\hat{\mathbf{S}}$  will be calculated, with the ultimate goal of finding an equation of motion. Together with the time dependent wave function  $\Psi(t)$  and its hermitian conjugate  $\Psi^\dagger(t)$  the expectation value is defined as

$$\langle \hat{\mathbf{S}} \rangle = \int \Psi^\dagger \hat{\mathbf{S}} \Psi dx^3 \quad , \quad (3.6)$$

where integration is carried out over the whole space. Further calculating the total derivative of  $\langle \hat{\mathbf{S}} \rangle$  with respect to time  $t$  and using the fact, that the Pauli matrices and therefore the spin operator  $\hat{\mathbf{S}}$  is time independent  $\frac{\partial \hat{\mathbf{S}}}{\partial t} = 0$ , equation (3.6) reads

$$\begin{aligned} \frac{d\langle \hat{\mathbf{S}} \rangle}{dt} &= \frac{d}{dt} \int \Psi^\dagger \hat{\mathbf{S}} \Psi dx^3 \\ &= \int \left( \frac{\partial \Psi^\dagger}{\partial t} \right) \hat{\mathbf{S}} \Psi dx^3 + \int \cancel{\Psi^\dagger \left( \frac{\partial \hat{\mathbf{S}}}{\partial t} \right) \Psi} dx^3 + \int \Psi^\dagger \hat{\mathbf{S}} \left( \frac{\partial \Psi}{\partial t} \right) dx^3 \quad . \end{aligned} \quad (3.7)$$

Recalling the time dependent form of Schrödinger's equation

$$\hat{\mathcal{H}}|\Psi\rangle = i\hbar\frac{\partial}{\partial t}|\Psi\rangle \quad , \quad (3.8)$$

rearranging it to get an expression for  $\frac{\partial \Psi}{\partial t}$  and substituting this into equation (3.7) yields

$$\begin{aligned} \frac{d\langle \hat{\mathbf{S}} \rangle}{dt} &= \int \left( -\frac{1}{i\hbar} \Psi^\dagger \hat{\mathcal{H}}^\dagger \right) \hat{\mathbf{S}} \Psi dx^3 + \int \Psi^\dagger \hat{\mathbf{S}} \left( \frac{1}{i\hbar} \hat{\mathcal{H}} \Psi \right) dx^3 \\ &= \frac{1}{i\hbar} \int \Psi^\dagger \left( \hat{\mathbf{S}} \hat{\mathcal{H}} - \hat{\mathcal{H}} \hat{\mathbf{S}} \right) \Psi dx^3 \quad , \end{aligned} \quad (3.9)$$

where the hermitian character of the hamiltonian ,  $\hat{\mathcal{H}}^\dagger = \hat{\mathcal{H}}$ , is used in the last step. With the help of the commutator relation for two operator valued quantities  $\hat{\mathbf{S}}\hat{\mathcal{H}} - \hat{\mathcal{H}}\hat{\mathbf{S}} = [\hat{\mathbf{S}}, \hat{\mathcal{H}}]$ , this can be rewritten into

$$\frac{d\langle \hat{\mathbf{S}} \rangle}{dt} = \frac{1}{i\hbar} \langle [\hat{\mathbf{S}}, \hat{\mathcal{H}}] \rangle \quad . \quad (3.10)$$

Equation (3.10) is generally known as the Ehrenfest theorem for a time independent operator, in this case the spin operator  $\hat{\mathbf{S}}$ . Inserting Eq. (3.4) and Eq. (3.5) into Eq. (3.10) and exploiting the commutator relation for the Pauli matrices

$$[\sigma_i, \sigma_j] = 2i\epsilon_{ijk}\sigma_k \quad (3.11)$$

leads to the sought equation of motion in its final form

$$\frac{d\langle\hat{\mathbf{S}}\rangle}{dt} = \frac{g_e\mu_0\mu_B}{\hbar}\mathbf{H} \times \langle\hat{\mathbf{S}}\rangle \quad . \quad (3.12)$$

Executing the transition to the classical regime, i.e. leaving the discrete realm and going to the continuous one by letting  $\hbar \rightarrow 0$  going to zero while at the same time identifying the expectation value of the spin operator with the magnetization  $\langle\hat{\mathbf{S}}\rangle \rightarrow \mathbf{M}$  and using the definition of the gyromagnetic ratio

$$\gamma = \frac{g_e\mu_0\mu_B}{\hbar} \quad , \quad (3.13)$$

with  $\gamma > 0$ , Eq. (3.12) reads

$$\frac{d\mathbf{M}}{dt} = -\gamma\mathbf{M} \times \mathbf{H}_{\text{eff}} \quad . \quad (3.14)$$

Thus, together with the substitution of the external magnetic field into an effective field term,  $\mathbf{H} \rightarrow \mathbf{H}_{\text{eff}}$ , as it is done in the famous paper of Landau and Lifshitz [10], a classical equation of motion describing the interaction of a micromagnetic spin with an effective field is found.

Analyzing the structure of Eq. (3.14) yields two eminent results. First, the magnetization's motion is always perpendicular to the effective field. Second, having an effective field antiparallel to the magnetization does not lead to magnetization reversal, since  $\frac{d\mathbf{M}}{dt} = 0$ . Therefore, for the case of an external field  $\mathbf{H}_{\text{eff}} = \mathbf{H}$ , changing the direction of  $\mathbf{H}$  from parallel to antiparallel, with respect to the magnetization  $\mathbf{M}$ , Eq. (3.14) only describes a directional change of the precessional motion of the magnetization around the effective field. No magnetization reversal, opposed to what is observed for sufficiently strong fields, can be achieved with the presented formalism. Furthermore, this precession is an energy conserving motion and Eq. (3.14) does not include a mechanism to account for losses. Hence, several refinements of Landau and Lifshitz's equation have been proposed to account for these losses.

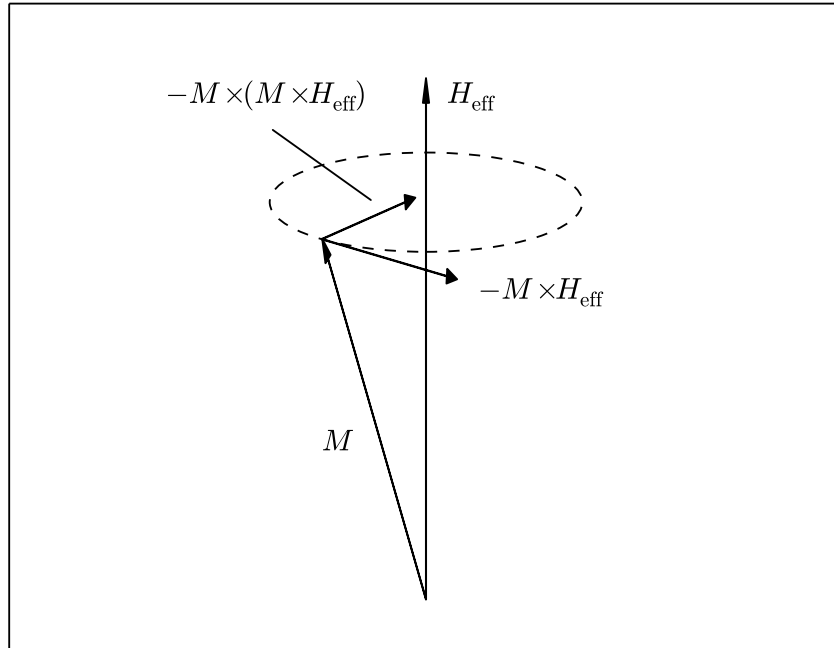


Figure 8: Illustration of the damped precession of the magnetization  $\mathbf{M}$  in an effective field  $\mathbf{H}_{\text{eff}}$  as described by the LLG equation (3.17).

### 3.2 Landau-Lifshitz-Gilbert Equation

A phenomenological damping term, that considers losses, is proposed by Landau and Lifshitz [10], but only works well for small damping and fails for systems with large damping. In order to compensate for this lack, another phenomenological damping term is suggested by Gilbert [12]

$$\mathcal{D} = \frac{\alpha}{M_s} \mathbf{M} \times \frac{\partial \mathbf{M}}{\partial t} \quad , \quad (3.15)$$

where  $M_s$  is the saturation magnetization and  $0 < \alpha \leq 1$  is the Gilbert damping factor. In order to get the explicit form of the damping term Eq. (3.15), replacing the partial derivative on the right-hand side of Eq. (3.17) with Eq. (3.17) yields together with the vector calculus identity  $\mathbf{a} \times (\mathbf{b} \times \mathbf{c}) = \mathbf{b}(\mathbf{a} \cdot \mathbf{c}) - \mathbf{c}(\mathbf{a} \cdot \mathbf{b})$  and  $\mathbf{M} \frac{\partial \mathbf{M}}{\partial t} = 0$  the sought expression

$$\mathcal{D} \propto -\mathbf{M} \times \mathbf{M} \times \mathbf{H}_{\text{eff}} \quad . \quad (3.16)$$

Figure 8 displays the damped precession described by the Landau-Lifshitz-Gilbert equation, Eq. (3.17). The first term,  $-\mathbf{M} \times \mathbf{H}_{\text{eff}}$ , describes the precessional motion around

the effective field. The second term, also called Gilbert damping term, Eq. (3.16), is constructed in such a way, that its motion is always perpendicular to the precessional vector as well as to the magnetization's vector and points towards the field vector. Thus the damping term enables the modeling of losses, invoked through e.g. eddy currents in ferromagnetic metals, which allow the magnetization to align with the effective field. Through the combination of the undamped Landau-Lifshitz equation (3.14) with Gilbert's damping term (3.15) the well known Landau-Lifshitz-Gilbert equation (LLG) in its compact form can be written as

$$\begin{aligned} \frac{\partial \mathbf{M}}{\partial t} &= -\gamma \mathbf{M} \times \mathbf{H}_{\text{eff}} + \mathcal{D} \\ &= -\gamma \mathbf{M} \times \mathbf{H}_{\text{eff}} + \frac{\alpha}{M_s} \mathbf{M} \times \frac{\partial \mathbf{M}}{\partial t} \quad . \end{aligned} \quad (3.17)$$

### 3.3 The Effective Field $\mathbf{H}_{\text{eff}}$

Following Gilbert's derivation of the LLG [12], the effective field is equal to the functional derivative of an effective potential energy term

$$\mathbf{H}_{\text{eff}}(\mathbf{r}, t) = -\frac{1}{\mu_0} \frac{\delta E_{\text{eff}}[\mathbf{M}(\mathbf{r}, t)]}{\delta \mathbf{M}(\mathbf{r}, t)} \quad . \quad (3.18)$$

Depending on the system under investigation, different energy terms contribute to  $E_{\text{eff}}$ . In the following, only energy terms relevant for this thesis will be discussed. The total effective energy for the proposed sensor consists of four energy contributors

$$E_{\text{eff}} = E_{\text{an}} + E_{\text{ex}} + E_{\text{st}} + E_{\text{ze}} \quad , \quad (3.19)$$

the anisotropy energy  $E_{\text{an}}$ , the exchange energy  $E_{\text{ex}}$ , the stray field energy  $E_{\text{st}}$  and the Zeeman energy  $E_{\text{ze}}$ .

### 3.4 Anisotropy-Field Energy

Due to interactions between inhomogeneously distributed spins and charge clouds with electrostatic fields of their neighbouring atoms, the magnetization's freedom to lie in an arbitrary direction becomes constrained by the crystal's lattice structure. Thus, hard and easy directions in the crystal arise, whereas the magnetization tends to lie along an easy axis [13]. A measure of how strong the magnetization tends to align with an easy direction is given by an anisotropy constant  $K$ . For the purpose of the presented thesis

two types of anisotropy, the uniaxial crystalline anisotropy  $K_1$  and the shape anisotropy  $K_{\text{sh}}$ , are considered. The proposed sensor exhibits perpendicular uniaxial anisotropy, with respect to the plane of the layers. While the shape anisotropy for thin oblate ellipsoid films favours the magnetization to lie in-plane, perpendicular anisotropy can be achieved through growth of an oriented film with a perpendicular crystalline anisotropy [14]. The energy due to magneto crystalline anisotropy [15] reads

$$\epsilon_c = E_c/V = K_1 \sin^2(\theta) + \mathcal{O}(\sin^4(\theta)) \quad , \quad (3.20)$$

where  $\theta$  is the angle between the direction of magnetization and the easy direction and  $V$  is the film volume. Equation (3.20) neglects higher order terms, since they usually are small corrections to the first term. The even character of this ansatz arises due to symmetry considerations, where the energy for the magnetization parallel to the easy axis must be the same as for the antiparallel case. The contribution of shape anisotropy energy can be given by the magnetostatic energy of a uniformly magnetized ferromagnetic ellipsoid through

$$\epsilon_{\text{sh}} = K_{\text{sh}} = E_{\text{sh}}/V = \frac{1}{2}\mu_0 N M_s^2 \quad . \quad (3.21)$$

Here  $\mu_0$ ,  $M_s$  and  $N$  are the magnetic field constant, the saturation magnetization and the demagnetizing factor. The demagnetizing factor for a thin-film with magnetization perpendicular to plane is given by  $N = 1$  [14]. Thus the total anisotropy energy density is

$$\begin{aligned} \epsilon_{\text{an}} &= \epsilon_c + \epsilon_{\text{sh}} \\ &= K_1 \sin^2(\theta) + \frac{1}{2}\mu_0 M_s^2 \cos^2(\theta) \quad . \end{aligned} \quad (3.22)$$

As a result of this, perpendicular anisotropy can only be achieved if

$$K_1 > \frac{1}{2}\mu_0 M_s^2 \quad (3.23)$$

holds true. For the sensor's fixed layer with a saturation magnetization of  $M_s = 7.1 \times 10^5 \text{ A m}^{-1}$  and the magnetic constant  $\mu_0 = 1.3 \times 10^{-6} \text{ T m A}^{-1}$ , the shape anisotropy equals  $K_{\text{sh}} = 3.3 \times 10^5 \text{ J/m}^3$ . Comparison of this result with the fixed layer's crystalline anisotropy of  $K_c = 1.3 \times 10^6 \text{ J/m}^3$  shows a ratio of  $K_{\text{sh}}/K_c \approx 10\%$ . In case of the free layer, which exhibits a crystalline anisotropy of  $K_c = 5.3 \times 10^5 \text{ J/m}^3$ , the ratio is

$K_{\text{sh}}/K_{\text{c}} \approx 62\%$ , revealing an easier switching character due to similar magnitudes of the involved anisotropies. Since the shape anisotropy tries to turn the magnetization away from the designed perpendicular anisotropy, an effective, reduced uniaxial anisotropy constant  $K_{\text{uni}} = K_{\text{c}} - K_{\text{sh}}$  can be defined

$$K_{\text{uni}} = \begin{cases} 2 \times 10^5 \text{ J/m}^3 & \text{Free Layer} \\ 1 \times 10^6 \text{ J/m}^3 & \text{Fixed Layer} \end{cases} . \quad (3.24)$$

Another important quantity in the context of anisotropy is the so-called anisotropy field  $\mathbf{H}_{\text{a}}$ . This field limits the achievable coercivities for a ferromagnetic layer, since it describes the necessary field strength to rotate the magnetization into saturation along a hard axis. It can easily be derived from the energy density for the magnetization  $\mathbf{M}$  of a ferromagnetic sample of uniaxial anisotropy  $K_{\text{uni}}$ , that is under the effect of a magnetic field  $\mathbf{H}_{\text{a}}$

$$\epsilon = K_{\text{uni}} \sin^2 \theta - \mu_0 M_{\text{s}} H_{\text{a}} \cos(\eta - \theta) \quad , \quad (3.25)$$

with  $\theta$  and  $\eta$  being the angles between  $\mathbf{M}$  and the easy axis, and  $\mathbf{H}_{\text{a}}$  and the easy axis, respectively. Choosing  $\eta = \pi/2$  to satisfy the hard axis condition for  $\mathbf{H}_{\text{a}}$ , minimizing Eq. (3.25),  $\frac{\partial \epsilon}{\partial \theta} = 0$  with respect to  $\theta$  and using the equality  $\sin(\pi/2 - \theta) = \cos(\theta)$  gives

$$\begin{aligned} \frac{\partial \epsilon}{\partial \theta} = 0 &= 2K_{\text{uni}} \sin(\theta) \cos(\theta) - \mu_0 M_{\text{s}} H_{\text{a}} \sin(\pi/2 - \theta) \\ H_{\text{a}} &= \frac{2K_{\text{uni}}}{\mu_0 M_{\text{s}}} \sin(\theta) \quad , \end{aligned} \quad (3.26)$$

which has its maximum value for  $\sin(\theta) = 1$ , or  $\theta = \pi/2$ . It is noteworthy, that the denominator is an important quantity for ferromagnets, which is well known as saturation polarization  $J_{\text{s}} = \mu_0 M_{\text{s}}$ . A sketch of the described system is depicted in Fig. 9.

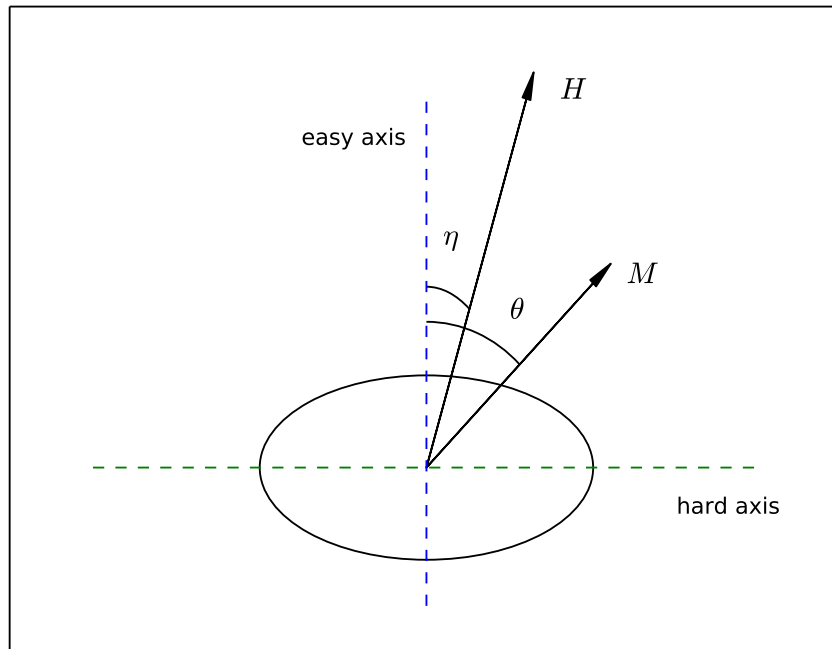


Figure 9: Sketch of an elliptical thin-film with uniaxial anisotropy perpendicular to plane. Angles are named as used for the energy density ansatz in Eq. (3.25). When compared with a typical Stoner Wolfarth particle of the same shape, the easy axis would change places with the hard axis and thus the magnetization would tend to lie in-plane, instead of perpendicular to plane.

### 3.5 Exchange-Field Energy

It is well known that ferromagnetic materials prefer to be in a magnetically ordered state. For temperatures lower than the Curie temperature,  $T < T_C$ , this phenomenon is called spontaneous magnetization. A ferromagnet can also show this behaviour for temperature higher than room temperature,  $T_R < T < T_C$ . The origin for this behaviour lies within quantum mechanical exchange interactions, independently described by Dirac [16] and Heisenberg [17], that couple electrons over a large distance. In the following, a brief sketch of the derivation of the Heisenberg hamiltonian (3.32), conducted in [18], will be given. The simple case of a two electron system in their Coulomb potential is described by the Coulomb hamiltonian

$$\hat{\mathcal{H}}_{\text{Coulomb}} = \sum_i^2 \frac{p_i^2}{2m} + V(\mathbf{r}_1, \mathbf{r}_2) \quad , \quad (3.27)$$

which does not include any spin dependency. An extension of this hamiltonian can be achieved through addition of an exchange term, that couples both spins in a simple way,

$$\hat{\mathcal{H}}_{\text{Spin}} = A \hat{S}_a \cdot \hat{S}_b \quad , \quad (3.28)$$

where  $\hat{S}_a, \hat{S}_b$  are the spin operators of both electrons and  $A$  is a generic coupling constant. Since electrons are fermions with spin  $1/2$ , the two electron system has a total spin of  $S = 1$  or  $S = 0$ , which is referred to as the triplet and singlet state, respectively. Thus, the electron wave functions can be written as a combination of a spin dependent  $|\chi\rangle$  and a spin independent  $|\psi\rangle$  part for the singlet  $|\psi\rangle_s$  and triplet  $|\psi\rangle_t$  state

$$|\psi\rangle_s = |\chi\rangle_s |\psi\rangle \quad \quad \quad |\psi\rangle_t = |\chi\rangle_t |\psi\rangle \quad . \quad (3.29)$$

Application of the Coulomb hamiltonian on both wave functions yields the eigenvalues  $E_s$  and  $E_t$

$$\hat{\mathcal{H}}_{\text{Coulomb}} |\psi\rangle_s = E_s |\psi\rangle_s \quad \quad \quad \hat{\mathcal{H}}_{\text{Coulomb}} |\psi\rangle_t = E_t |\psi\rangle_t \quad (3.30)$$

$$= (U + \mathcal{J}) |\psi\rangle_s \quad \quad \quad = (U - \mathcal{J}) |\psi\rangle_t \quad , \quad (3.31)$$

where  $U$  is the energy attributed to the Coulomb interaction and  $\mathcal{J}$  is the so called exchange integral, describing the spin coupling. Taking this result for a two electron

system and expanding it to a  $N$  multi electron system yields the Heisenberg hamiltonian

$$\hat{\mathcal{H}}_{\text{Heisenberg}} = - \sum_{i < j} \mathcal{J}_{ij} \hat{S}_i \hat{S}_j \quad . \quad (3.32)$$

This hamiltonian assumes pairwise interactions of electrons  $i, j$  with the appropriate exchange interaction  $\mathcal{J}$ . In many cases  $\mathcal{J}$  is taken as constant between direct neighbours and next to direct neighbours, and zero for all other combinations  $i < j$ . It is interesting to note, that a positive exchange interaction  $\mathcal{J} > 0$  leads to ferromagnetic behaviour, while a negative one leads to anti ferromagnetic states. Equation (3.32) is the starting point to calculate the exchange field, needed for a micromagnetic description. This transformation is given in e.g. [19] and results in the following expression for the exchange field

$$\mathbf{H}_{\text{ex}}(\mathbf{r}) = \frac{2A_{\text{ex}}}{\mu_0 M_s} \nabla^2 \mathbf{M}(\mathbf{r}) \quad , \quad (3.33)$$

with  $A_{\text{ex}}$  being a material specific exchange constant.

### 3.6 Stray-Field Energy

The third contribution to the effective energy is the stray-field energy or demagnetizing-field energy. It describes the energy of the magnetic field that is generated by the sample's magnetization itself, and can therefore be seen as a self-energy term. This energy originates from a pairwise dipole-dipole interaction of atomic moments  $\mathbf{m}(\mathbf{r}_i), \mathbf{m}(\mathbf{r}_j)$ . The stray field can be written as

$$\mathbf{H}_{\text{st}}(\mathbf{r}) = - \frac{1}{\mu_0} \frac{\partial E_{\text{st}}}{\partial \mathbf{M}} = \int_V \mathcal{N}(\mathbf{r} - \mathbf{r}') \mathbf{M}(\mathbf{r}') d^3 r' \quad , \quad (3.34)$$

with the integral being carried out over the sample's volume  $V$  and  $\mathcal{N}(\mathbf{r} - \mathbf{r}')$  being the  $3 \times 3$  dimensional demagnetization tensor field. Integration of  $\mathbf{H}_{\text{st}}(\mathbf{r})$  with respect to  $\mathbf{M}$ , by inverting relation (3.18), yields the energy associated with the stray field

$$E_{\text{st}} = - \frac{\mu_0}{2} \int_V \int_V \mathbf{M}(\mathbf{r}) \mathcal{N}(\mathbf{r} - \mathbf{r}') \mathbf{M}(\mathbf{r}') d^3 r d^3 r' \quad . \quad (3.35)$$

### 3.7 Zeeman-Field Energy

As last contribution, the potential energy of a magnetized body under the effect of an external field  $\mathbf{H} = \mathbf{H}_{ze}$  is given by the following expression

$$E_{ze} = -\mu_0 \int_V \mathbf{H}_{ze}(\mathbf{r}) \mathbf{M}(\mathbf{r}) d^3r \quad . \quad (3.36)$$

### 3.8 Stochastic Landau-Lifshitz-Gilbert Equation

The former introduced LLG, Eq. (3.17), describes magnetization dynamics of a deterministic system. Thermal fluctuations though play an important roll for magnetization reversal processes and thus have to be included into the description. This can be done, by adding a field term, the thermal field  $\mathbf{H}_{th}$ , to the effective field  $\mathbf{H}_{eff}$ . The modified LLG equation therefore takes the new form

$$\begin{aligned} \frac{\partial \mathbf{M}}{\partial t} &= -\gamma \mathbf{M} \times (\mathbf{H}_{eff} + \mathbf{H}_{th}) + \frac{\alpha}{M_s} \mathbf{M} \times \frac{\partial \mathbf{M}}{\partial t} \\ \frac{\partial \mathbf{M}}{\partial t} &= -\gamma' \mathbf{M} \times (\mathbf{H}_{eff} + \mathbf{H}_{th}) - \frac{\alpha \gamma'}{M_s} \mathbf{M} \times (\mathbf{M} \times (\mathbf{H}_{eff} + \mathbf{H}_{th})) \quad , \end{aligned} \quad (3.37)$$

where the second equation with  $\gamma' = \gamma/(1+\alpha^2)$  represents its explicit form. The thermal field  $\mathbf{H}_{th}$  is assumed to be non correlated in space and time, with its variance  $D$  being determined by the fluctuation dissipation theorem

$$\langle H_{th,i}(\mathbf{r}, t) H_{th,j}(\mathbf{r}', t') \rangle = 2D \delta_{ij} \delta(\mathbf{r} - \mathbf{r}') \delta(t - t'), \quad (3.38)$$

$$\text{with } D = \frac{\alpha k_B T}{\gamma \mu_0^2 M_s V} \quad . \quad (3.39)$$

Also the average

$$\langle H_{th,i}(\mathbf{r}, t) \rangle = 0 \quad (3.40)$$

for each component of  $\mathbf{H}_{th}$  has to vanish. Thus, the thermal field can be modelled as a Gaussian random process, describing thermal fluctuations or thermal noise in a sensor, which is why it is often called Gaussian white noise. For more detailed information about the mathematical implementation for simulation purposes, the reader is referred to e.g. [20].

### 3.9 The Spin-Diffusion Model

It was a very impactful finding, that a spin polarized current exerts a torque, the so-called spin-torque, on a given magnetization distribution. Two well known models, the one proposed by Slonczewski [21] and the other presented by Zhang and Li [22], describe different aspects of spin-torque effects. The model of Slonczewski shows good results for magnetic multilayer structures that consist of a free layer separated from a fixed layer, in which the spin polarization takes place, but is unfit to describe spin-torque effects for smoothly varying magnetization distributions. Fortunately, Zhang and Li's model compliments Slonczewski's model by introducing a mechanism, that is able to describe domain wall movement, i.e. slowly varying magnetization configurations. Though, due to this model's assumption of vanishing gradients of the spin accumulation  $\nabla \mathbf{s} = 0$ , it fails to describe transitions between different layers in a multilayer stack. However, the model of choice used to describe spin-torque effects in the thesis at hand, is a spin-diffusion model implemented by Abert et al. [23]. It is shown in another work by Abert et al. [24], that their model is able to reproduce the results from Zhang and Li as well as those from Slonczewski. The modified LLG equation, extended by the spin accumulation  $\mathbf{s}$ , takes the following form

$$\frac{\partial \mathbf{M}}{\partial t} = -\gamma \mathbf{M} \times \left( \mathbf{H}_{\text{eff}} + \frac{J}{\hbar \gamma M_s} \mathbf{s} \right) + \frac{\alpha}{M_s} \mathbf{M} \times \frac{\partial \mathbf{M}}{\partial t} \quad , \quad (3.41)$$

where  $\gamma$  is the gyromagnetic ratio,  $\hbar$  is the reduced Planck constant,  $J$  is the exchange strength between itinerant and localized spins,  $\alpha$  is the Gilbert damping,  $\mathbf{H}_{\text{eff}}$  is the effective field,  $M_s$  is the saturation magnetisation and  $\mathbf{M}$  is the magnetization. The spin accumulation has to satisfy a diffusion equation of the form

$$\frac{\partial \mathbf{s}}{\partial t} = -\nabla \cdot \mathbf{j}_s - \frac{\mathbf{s}}{\tau_{\text{sf}}} - J \frac{\mathbf{s} \times \mathbf{m}}{\hbar} \quad . \quad (3.42)$$

The first term on the right-hand side of Eq. (3.42) can be understood as a source term, that generates spin accumulation at interfaces in a multi layer stack, where  $\mathbf{j}_s$  denotes the spin-current. The second term  $-\mathbf{s}/\tau_{\text{sf}}$  accounts for an exponential decay of  $\mathbf{s}$  into the bulk of a layer, with the spin-flip relaxation time  $\tau_{\text{sf}}$ . Eventually, the third term shows the spin-torque, acting on the normalized magnetization  $\mathbf{m}$ . The spin accumulation can be determined for a given electric current  $\mathbf{j}_e$  and the spin-current

$$\mathbf{j}_s = \beta \frac{\mu_B}{e} \mathbf{m} \otimes \mathbf{j}_e - 2D_0 \left[ \nabla \mathbf{s} - \beta \beta' \mathbf{m} \otimes \left( (\nabla \mathbf{s})^T \mathbf{m} \right) \right] \quad , \quad (3.43)$$

where  $\beta$  and  $\beta'$  are dimensionless polarization parameters,  $D_0$  is the diffusion constant,  $\mu_B = e\hbar/2m_e$  is the Bohr magneton and  $e$  is the electron charge. The first term on the right-hand side in Eq. (3.43) shows the interaction between the  $\mathbf{j}_e$  and  $\mathbf{m}$  and can be regarded as the spin-current generation term. An example of the spin-accumulation

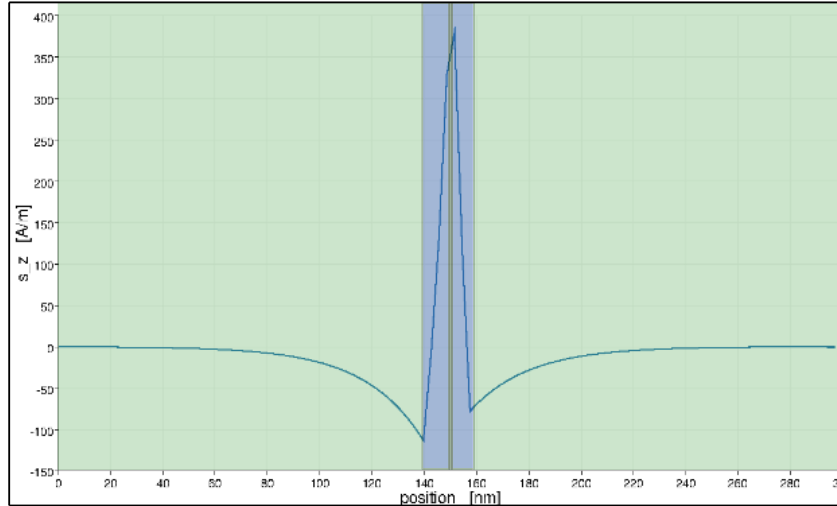


Figure 10: The z-component of the spin accumulation throughout a multi layer stack is depicted for an antiparallel state. From left to right, the color coded layers are: contact/fixed/spacer/free/contact.

distribution of the z-component throughout a multilayer stack is shown in Fig. 10 for an antiparallel state. The peaks near the interfaces show that spin accumulation indeed is generated at interfaces between thin-films. From left to right, the coloured regions depict the contact/fixed/spacer/free/contact layers. The exponential decay of  $\mathbf{s}$  into the contact regions is clearly visible.

### 3.10 Energy Barrier and Thermal Stability

When dealing with switching processes that are subject to thermal fluctuation, it becomes important to investigate the thermal stability of the different layers, especially the free layer. The free layer can be in one of the two possible states, parallel or antiparallel, associated with energies  $E_1$  and  $E_2$ , respectively, with  $0 < E_1, E_2 < E_{\max}$ . If there is no external magnetic field present and the layer is considered to be treated at a temperature of  $T = 0$  K, the magnetization with an energy of  $E_1$  gets no stimulus to overcome the energy barrier  $E_{\max} = KV$ , with the effective anisotropy  $K$  and volume  $V$ , that separates it from switching to the other state with energy  $E_2$ . Adding an external

field can be described through a shift of both energy levels by a constant factor  $\epsilon > 0$  but in opposite directions. This results in bringing one state, e.g.  $E_1 + \epsilon$  closer to  $E_{\max}$  while moving the other one  $E_2 - \epsilon$  further away from  $E_{\max}$  due to the fact that the external field, in this case, stabilizes the antiparallel configuration and destabilizes the parallel one. However, these newly accomplished energy states are still considered stable as long as  $\Delta E_1, \Delta E_2 < E_{\max}$ , with  $\Delta E_1 = E_{\max} - (E_1 + \epsilon)$  and  $\Delta E_2 = E_{\max} - (E_2 - \epsilon)$  holds true. Now with the addition of a temperature  $T > 0$  K to the system, the thermal energy  $k_B T$ , with  $k_B$  being Boltzmann's constant, has to be considered. As soon as the thermal energy exceeds the remaining difference between a state's energy and the maximum energy,  $\Delta E_1 + k_B T, \Delta E_2 + k_B T > E_{\max}$ , thermally activated switching is possible. Since thermally activated switching is a statistical process, a probability for the magnetization to retain its magnetization can be given by

$$P(t) = e^{-t/\tau} \quad , \quad (3.44)$$

where  $t$  is the time passed and  $\tau$  is the inverse switching rate. The switching rate  $\tau$  is described by the Arrhenius or Néel-Brown law,

$$\tau(T, H) = \tau_0 \exp(E(H)/k_B T) \quad (3.45)$$

with the attempt frequency  $\tau_0$ , the temperature  $T$  and the external field  $H$  dependent energy barrier  $E(H) = E_{\max}$ , [25]. Since the free layer can be treated as a single domain particle, its energy barrier can be written as

$$E(H) = KV(1 - H/H_{sw})^2 \quad , \quad (3.46)$$

as given in [26]. Here  $V$  is the layer's volume,  $K$  is the effective anisotropy, which is the sum of the shape anisotropy and the uniaxial anisotropy,  $H$  is the effective field parallel to the easy axis and  $H_{sw} = H_{ani}$  is the switching field, or anisotropy field. Equation (3.46) implies, that for  $H = H_{sw}$  the energy barrier is vanishing and magnetization reversal takes place.

Taking a closer look at the exponent in Eq. (3.45),  $E(H)/k_B T$  represents the ratio of the energy barrier and the thermal activation energy. The larger it becomes, the more likely it is that the ferromagnetic layer retains its current magnetization direction and likewise the less likely it is that thermally induced switching occurs. For the purpose of the proposed sensor model, an energy ratio of  $\alpha = E(H)/k_B T = 70$  is chosen, to guarantee

good long term stabilization, compared to a magnetic tunnel junction's (MTJ) energy ratio of  $\alpha \approx 40$ , which is sufficient for a ten year data retention time [27].

## 4 Numerical Simulations

### 4.1 Deterministic Simulations with Simplified Model

#### 4.1.1 Single Free Layer

In order to demonstrate the basic working principle of the proposed sensor concept, a simplified model that neglects statistical influences caused by thermal fluctuations is considered. The first issue of interest is to determine the sensor's sensitivity  $S$ . In order to achieve this goal, the applied simplifications will be described in detail in the following.

The first and most important step is to eliminate thermal fluctuations of the magnetization configuration. These fluctuations can be avoided by setting the temperature variable to  $T = 0$  K, which allows the simulations to be performed in a deterministic regime. The second assumption allows to reduce the reference layer, one conducting layer and the pinned layer of the sensor to only a single one, the so-called fixed layer. This fixed layer can be considered as a black box, where the inner structure, with the purpose of polarizing the spin-current, can be neglected. Furthermore, the demagnetizing field of the fixed layer acting on the free layer is set to zero. This can be argued for because a well designed sensor's demagnetizing field of the fixed layer (consisting of two antiparallel magnetic layers) should vanish in the region of the free layer. Simulations under the mentioned conditions have already been performed by Holzmann [28] in a preceding thesis. These findings clearly show a linear sensor gain  $S$  for both switching processes, with a stronger gain for switching from a parallel to an antiparallel state. For more details about these simulations, the reader is referred to the just mentioned thesis. During the studies on the z-field sensor, the used simulation tool *magnum.fe* received several refinements, which one of them included a change in simulation parameters as described in its manual [29] under section *spin diffusion*, in subsection *legacy material parameters*. The following relations hold true

$$\begin{aligned}\lambda_{sf} &= \sqrt{2D_0\tau_{sf}} \\ \lambda_j &= \sqrt{\frac{2D_0}{\hbar J}} \\ c &= \frac{J\mu_0}{\hbar\gamma M_s} .\end{aligned}$$

This set of equations relates the former used coupling constant  $c$ , the spin diffusion

---



---

	$a$ (Am <sup>-2</sup> T <sup>-1</sup> )	$\sigma_a$ (Am <sup>-2</sup> T <sup>-1</sup> )	$b$ (Am <sup>-2</sup> )	$\sigma_b$ (Am <sup>-2</sup> )
p → ap	$-2.01 \times 10^{13}$	$1.83 \times 10^{12}$	$9.47 \times 10^{12}$	$2.18 \times 10^{12}$
ap → p	$-3.11 \times 10^{12}$	$3.72 \times 10^{10}$	$-3.17 \times 10^{12}$	$4.44 \times 10^9$

---



---

Table 1: This table shows the fit parameters of equation (4.2) with their standard deviation for the data presented in Fig. 11.

lengths  $\lambda_{sf}$  and  $\lambda_j$  to the onwards used parameters  $J$ , the coupling strength and  $\tau_{sf}$ , the spin-flip relaxation time. Taking a closer look at these relations, an overdetermined system of equations concerning the coupling strength is found. Using the latter two equations, two different expressions  $J_1$  and  $J_2$  are obtained from which we can derive the mean

$$J = \frac{J_1 + J_2}{2} \quad (4.1)$$

for further use in all succeeding simulations.

Figure 11 represents the results after switching to the new parameter set in the spin-diffusion model. The switching-current density  $j_s$  plotted against the applied external field  $H_{\text{ext}}$  is depicted here. The dots mark the actual simulated switching-current densities at a given field value, while the straight lines show the calculated best fits to the switching events. The fit function is defined as follows

$$y(x) = xa + b \quad , \quad (4.2)$$

with  $a$  and  $b$  being the sensor's gain  $a = S$  and zero offset, respectively. Comparing these results to the ones obtained in the previous work of Holzmann [28], once more, a linear correspondence between the applied field and the switching-current densities is found, although the absolute values differ slightly. However, the important result is that the coefficient of variation  $c^v$ , Eq. (4.3), for the switching-current densities still is of the same order of magnitude, as can be seen in Tab. 2. Together with the standard deviation  $\sigma$  and the mean  $\mu$ , the coefficient of variation can be defined as

$$c_i^v = \frac{\sigma}{\mu} \quad , \quad (4.3)$$

with  $i = \{a, b\}$ .

	$ c_a^v $ (%) - new	$ c_b^v $ (%) - old
$p \rightarrow ap$	9	2
$ap \rightarrow p$	1	0

Table 2: This table shows the coefficients of variation derived from the results of Eq. (4.2), before (old) and after (new) the change of parameters in the spin-diffusion model, rounded to zero decimal places.

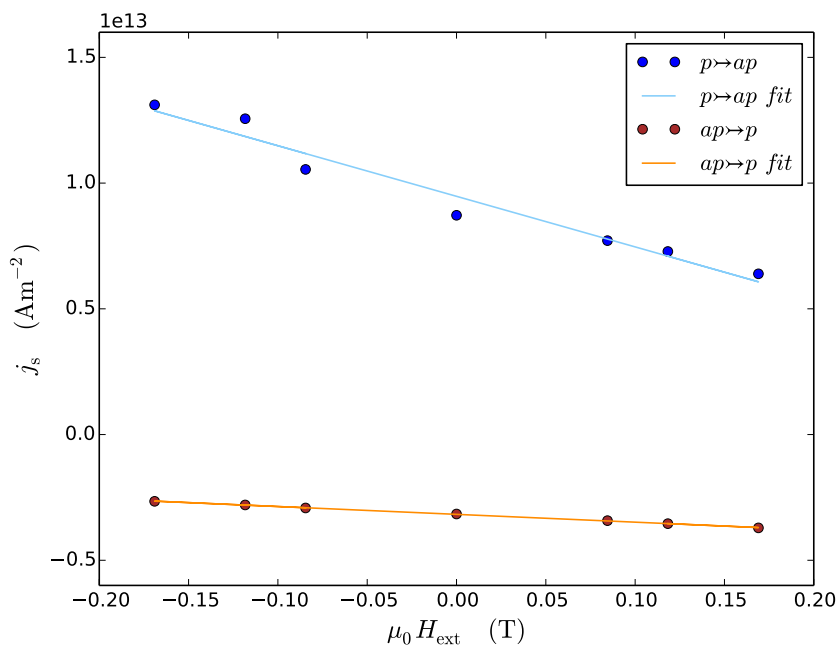


Figure 11: This figure shows switching-current densities  $j_s$  plotted against an external field  $\mu_0 H_{\text{ext}}$  (dots). The full lines represent the best linear fit to the data sets. Note, that current densities as well as the slope of the straight are higher when switching from parallel to antiparallel ( $p \rightarrow ap$ ) as compared to switching from antiparallel to parallel ( $ap \rightarrow p$ ).

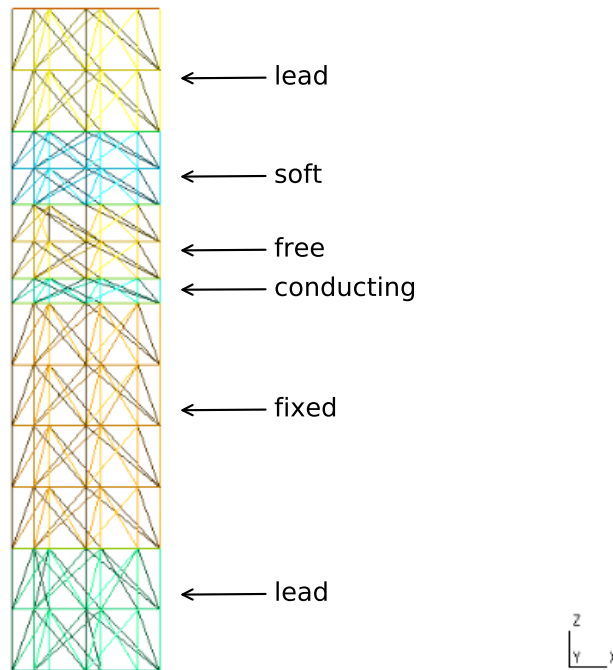


Figure 12: This figure shows a simplified version of the sensor with the different layers labelled. The coloured inner structure pictures the mesh with the horizontal lines indicating the discretization of the mesh. The additional soft layer can be either on top of, or beneath the free layer.

#### 4.1.2 Additional Soft Magnetic Layer

After getting preliminary data for the sensor's behaviour in an external magnetic field the next step is to find ways to improve the sensor, i.e. lower the switching-current densities in order to operate the sensor at lower currents, which would improve the operating costs, while at the same time it would help to keep the magnetic configuration of the fixed layer (or spin polarizer) more stable.

The following simplifications are applied in order to allow for reasonable simulation times. Figure 12 shows a model of the scaled sensor, where its diameter is set to a tenth of its original size, so that the radius reads  $R = 3$  nm. This allows to neglect the shape anisotropy effect, since it is small compared to the uniaxial anisotropy effect of

the sensor. Once more, the advantage of handling the spin polarizer as a black box with a zero demagnetizing field acting on the free layer, benefits the numerical experiment. That allows to neglect computation of magnetization dynamics within the fixed layer and their, per design vanishing, effect on the free layer. The magnetic interaction of the fixed layer with the external field  $H_{\text{ext}}$  must not be excluded though. In fact, the magnetic stiffness of this region is one of the limiting factors for the sensor, because as soon as the applied magnetic field overcomes the anisotropy field  $H_{\text{ani}}$ , the magnetization configuration of the fixed layer becomes unstable and thus the purpose of polarizing the current in a defined way would be lost. This shows, that the anisotropy field acts as an upper limit for the application of external fields. In order to avoid instabilities during the simulations, the maximum field strength  $H_{\text{max}}$  of the external field is set to one third of the anisotropy field

$$H_{\text{max}} = H_{\text{ext}}^{\text{max}} = \frac{1}{3}H_{\text{ani}} \quad . \quad (4.4)$$

The chosen method to reach lower switching-current densities here is to simply add an additional soft magnetic layer on top of or below the free layer, see Fig. 12. This should result in an easier to revert magnetic configuration. The pictorial point of view provides the following explanation: An ideal soft magnet possesses no crystalline or uniaxial anisotropy, so that  $K_{\text{uni}}^{\text{soft}} = 0$ . This allows for the magnetization to follow the direction of the applied field without having to overcome the threshold or anisotropy field, since  $H_{\text{ani}}^{\text{soft}} \propto K_{\text{uni}}^{\text{soft}} = 0$ . This results in a situation where not only the external field but also the soft magnetic layer adjacent to the free layer exert their force on the free magnetic layer. Under these combined forces the magnetization of the free layer is expected to change its direction quicker, without the use of stronger external fields or higher currents.

The theoretical approach explains the situation as follows: It has to be taken into account that magnetism is a quantum mechanical effect, since it deals with electron spins. Knowing that a material's magnetization is the sum of its spins and assuming pairwise spin interactions within a magnetic material, Heisenberg's Hamiltonian, Eq. (3.32), can be employed and it can be learned, that the spins and therefore the magnetization of the free and soft layer are exchange coupled. Once again, this leads to the conclusion, that an external field acting on the soft layer effectively spreads its force on the free layer. It can further be argued that the Heisenberg Hamiltonian does not suggest or imply any differentiation between magnetic domains as long as they are exchange coupled. So the addition of a soft layer adjacent to the free layer in fact means a simple enlargement of the free layer, accompanied by a change of the uniaxial anisotropy constant of the free

layer. Taking a closer look at Eq. (4.5), it can be seen that the addition of a soft layer adjacent to the free layer yields a larger combined free layer with a reduced uniaxial anisotropy constant  $K_{\text{uni}}^{\text{tot}}$ , that results in an easier to manipulate free layer.

$$\begin{aligned} K_{\text{uni}}^{\text{tot}} &= \frac{d^{\text{free}} \cdot K_{\text{uni}}^{\text{free}} + d^{\text{soft}} \cdot K_{\text{uni}}^{\text{soft}}}{d_{\text{tot}}} \\ d_{\text{tot}} &= d^{\text{free}} + d^{\text{soft}} \end{aligned} \quad (4.5)$$

Here,  $K_{\text{uni}}^{\text{free}}$  and  $K_{\text{uni}}^{\text{soft}}$  are the uniaxial anisotropy constants for the free and soft layer, respectively and  $K_{\text{uni}}^{\text{tot}}$  denotes the resulting anisotropy for the combined soft- plus free layer. The variables  $d^{\text{free}}$  and  $d^{\text{soft}}$  symbolize the height of the respective layer, which add up to the total size of the combined layer  $d_{\text{tot}}$  and take care of the right proportionality, since the height is the only varied quantity besides the uniaxial anisotropy constants.

Over the course of the simulations  $d^{\text{free}}$  is held at a constant value of  $d^{\text{free}} = 3$  nm, while the height of the soft layer  $d^{\text{soft}}$  is varied between  $d^{\text{soft}} = 0$  nm, 3 nm and 5 nm. To further confirm the assumption that the system of free and soft layer can be treated as one single object, the order in which both layers appear is changed. So in the first half of the experiments the combined free layer consists of the soft layer on top of the free layer, as shown in Fig. 12, while the opposite hold true for the second half. Figure 13 depicts a complete current-hysteresis loop for the case where the added soft layer has a height of  $d^{\text{soft}} = 3$  nm. The orange triangles resemble the case in which the soft layer connects to the free layer from beneath and the blue circles mark the curve in which the soft layer sits above the free layer. It immediately can be seen that for both cases the curves appear to be identical. Taking a closer look on the inset of Fig. 13 it reveals, that there is no significant difference between the two cases, even on a point per point evaluation. The same holds true for every other part of the hysteresis curve as well as for the experiments that were conducted with different heights of the soft layer. Although the order of the two layers does not matter, the resulting change in size and anisotropy constant of the combined free layer does indeed have an effect on the switching-current densities. Figure 14 shows three hysteresis curves for differing combined free layer sizes. The size specifications 0 nm, 3 nm and 5 nm refer to the extra height of the added soft layer, which result in a total size of the combined free layer of  $d_{\text{tot}} = d^{\text{free}} + d^{\text{soft}}$  with  $d^{\text{free}}$  being the height of the free layer ( $d^{\text{free}} = 3$  nm) and  $d^{\text{soft}} = 0$  nm, 3 nm and 5 nm. The circles show the case with the standard-size free layer of  $d^{\text{free}} = 3$  nm. Taking this curve as the reference, it is apparent that by enlarging the free layer while at the same time reducing its uniaxial anisotropy, the roots of the hysteresis curves shrink towards

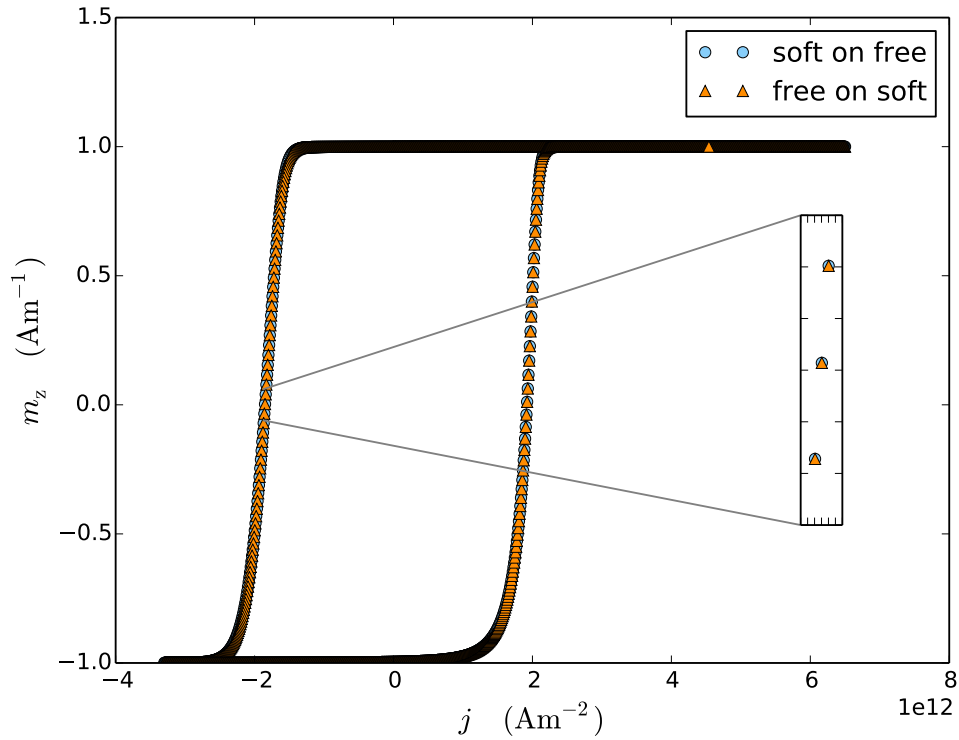


Figure 13: This figure shows the result for the two tested cases in which the additional soft magnetic layer once is placed on top of (soft on free) and then below (free on soft) the free layer. The normalized average magnetization of the z-component is plotted over the applied current density for the  $d^{\text{soft}} = 3$  nm high soft layer.

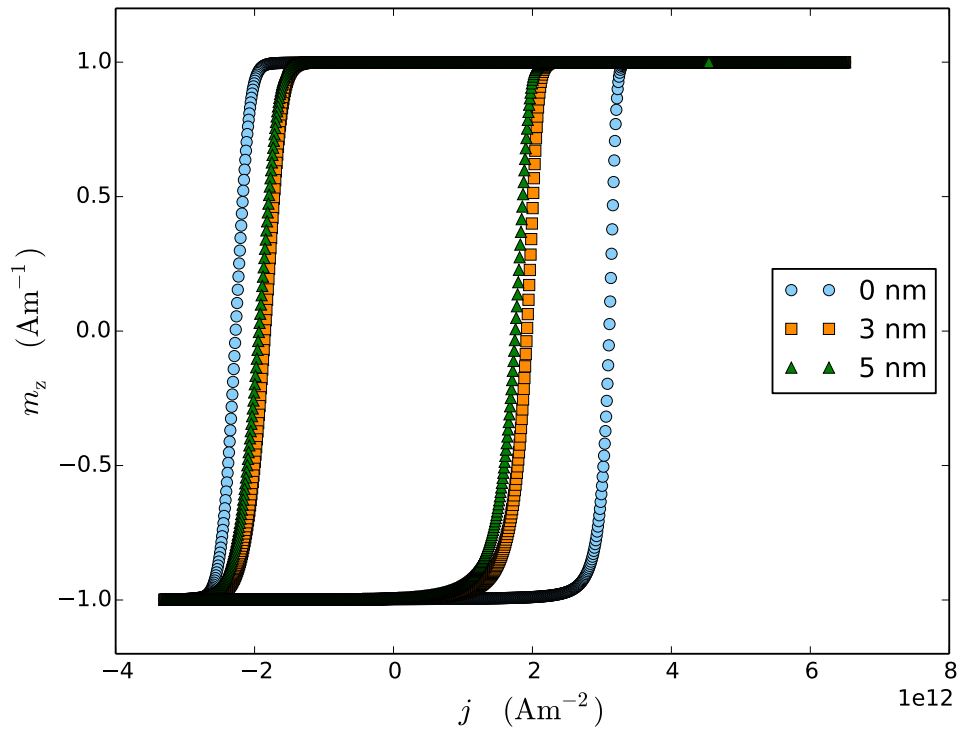


Figure 14: Hysteresis curves for three combined free layers ( $d_{\text{tot}} = d^{\text{free}} + d^{\text{soft}}$ ) of different heights, with  $d^{\text{free}} = 3 \text{ nm}$  and  $d^{\text{soft}} = 0 \text{ nm}, 3 \text{ nm}$  and  $5 \text{ nm}$ .

---

	0 nm $\rightarrow$ 3 nm	0 nm $\rightarrow$ 5 nm	3 nm $\rightarrow$ 5 nm
$p \rightarrow ap$	38%	43%	5%
$ap \rightarrow p$	18%	15%	3%

---

Table 3: Relative changes in switching-current densities due to an added soft magnetic layer adjacent to the free magnetic layer. 0 nm relates to the single free magnetic layer with a height of 3 nm, whereas 3 nm and 5 nm denote the combined free and soft layer, with the soft layer of respective size.

the origin, which results in lower switching-current densities  $j_s$ .

There are two additional facts to derive from these experiments. Firstly, when switching from a parallel state to an antiparallel state, higher currents are occurring. These higher currents, combined with the now easier to switch combined free layer, show a better improvement compared to the case in which lower currents are needed for the switching process. In Fig. 14, switching from  $p \rightarrow ap$  corresponds to the right side of the loop, whereas switching from  $ap \rightarrow p$  relates to the left side. Secondly, it can be seen, that the shift of the loops is asymmetrical. While for the  $p \rightarrow ap$  case there is a bigger shift in the switching-current density, the bigger the combined free layer gets, the opposite holds true for the  $ap \rightarrow p$  case. This can be explained as follows. The experiment was set up in such a way that in order to switch from  $ap \rightarrow p$  the current first has to pass through the spin polarizer and then it enters the free magnetic region. This leads to a situation in which, due to antiparallelism in the magnetic layers, the spin-torque accounts for a bigger part of the switching force. That allows the switching currents to generally be lower than the ones used to switch from  $p \rightarrow ap$ . Since the magnitude of the total spin-torque acting on the combined free layer without the support of a spin polarizing layer is smaller in the 3 nm case as compared to the 5 nm case, the switching current in turn needs to be higher for the 3 nm layer than for the 5 nm layer, see right slope of Fig. 14. In order to reverse the sensor's magnetic configuration back to its starting point, i.e. switching from  $ap \rightarrow p$ , the situation is a little different. The current now runs through the sensor, coming from the opposite side of the sensor. With a spin polarizer being in place on that end of the sensor, the spin-torque has a greater magnitude, thus allowing the switching current associated with the smaller layer to be smaller than the one related to the larger layer.

The results of the simulations are presented in Tab. 3. The first two columns contain the relative current reduction compared to the simple free layer which has a height of

3 nm but is referred to as 0 nm. In the last column the change of switching-current densities between the two compared additional soft layers in relation to the sole free layer is given. It should be noted that by doubling the size of the combined free layer, 0 nm  $\rightarrow$  3 nm, while making it softer at the same time yields the largest improvement for both cases,  $p \rightarrow ap$  and  $ap \rightarrow p$ . Given the fact, that switching from parallel to antiparallel uses higher currents it is well expected that the combined free layer has a stronger effect on the shift of switching-current densities for this case. For the examined changes of the combined free layer, this results in a current reduction of a maximum of 43% when switching from  $p \rightarrow ap$  and 15% when switching from  $ap \rightarrow p$ .

## 4.2 Stochastic Simulations

All of the prior simulations have been conducted in a deterministic regime. This allows to neglect the effect of stochastic fluctuations within the ferromagnetic layers. The focus of the following experiments lies exactly on those fluctuations of the magnetic configuration, so that the impact of thermal instabilities on the stiffness of the free layer and therefore the change in switching-current densities can be determined.

For this purpose, the sensor model gets simplified once more. Its general shape and structure stays as it has been introduced in Fig. 12, but for the soft layer. From bottom to top there are the lead-, fixed-, conductive-, free- and lead layers with respective heights of  $z = 5$  nm, 10 nm, 1 nm, 3 nm and 5 nm and a radius of  $r = 3$  nm. The fixed layer, or spin polarizer, is treated as unaffected by thermal fluctuations for switching purposes, since it is artificially designed to be much more rigid than the free layer. Also the demagnetizing field of the polarizer acting on the free layer is neglected during the simulation, since when properly designed, there should be a vanishing effect on the free layer. As a result of that, the LLG equation, Eq. (3.37), is only solved in the free layer's region and takes the exchange field-, the uniaxial anisotropy field-, the external field-, the spin-torque term and of course the thermal field term, as described in Sec. 3.8, into consideration.

Since the sensor is meant to operate at room temperature, a starting value of  $T = 290$  K is chosen. At this point the concept of energy barriers in magnetic layers gets important. These barriers, see Sec. 3.10, relate the magnetic energy of a layer with volume  $V$  and energy density  $K$  to the available thermal energy  $k_B T$  with  $k_B$  and  $T$  being Boltzmann's constant and temperature, respectively. It is necessary to overcome the energy barrier to switch from one state to the other. This means, the higher the barrier, the more energy has to be put into the system in order to induce magnetic reversal.

Figure 15 shows the result of 25 hysteresis cycles for an external field strength of  $H_{\text{ext}} = 0$  Am<sup>-1</sup> at room temperature of  $T = 290$  K. This temperature is sufficient to allow the magnetization to overcome energy barriers in the sensor. Therefore switching between the two states, parallel and antiparallel, is easily achieved for both directions due to thermal activation. This leads to standard deviations of  $\sigma_{\text{ap}} = 0.3 \times 10^{12}$  Am<sup>-2</sup> and  $\sigma_{\text{p}} = 0.7 \times 10^{12}$  Am<sup>-2</sup> and further translates into relative standard deviations of  $c_{\text{ap}} = 23\%$  and  $c_{\text{p}} = 70\%$  for switching from  $ap \rightarrow p$  and  $p \rightarrow ap$ , respectively. The significant difference between  $c_{\text{ap}}$  and  $c_{\text{p}}$  reflects the influence that spin polarization has on the applied current.

It is expected that switching from  $ap \rightarrow p$  requires lower switching currents, thus leav-

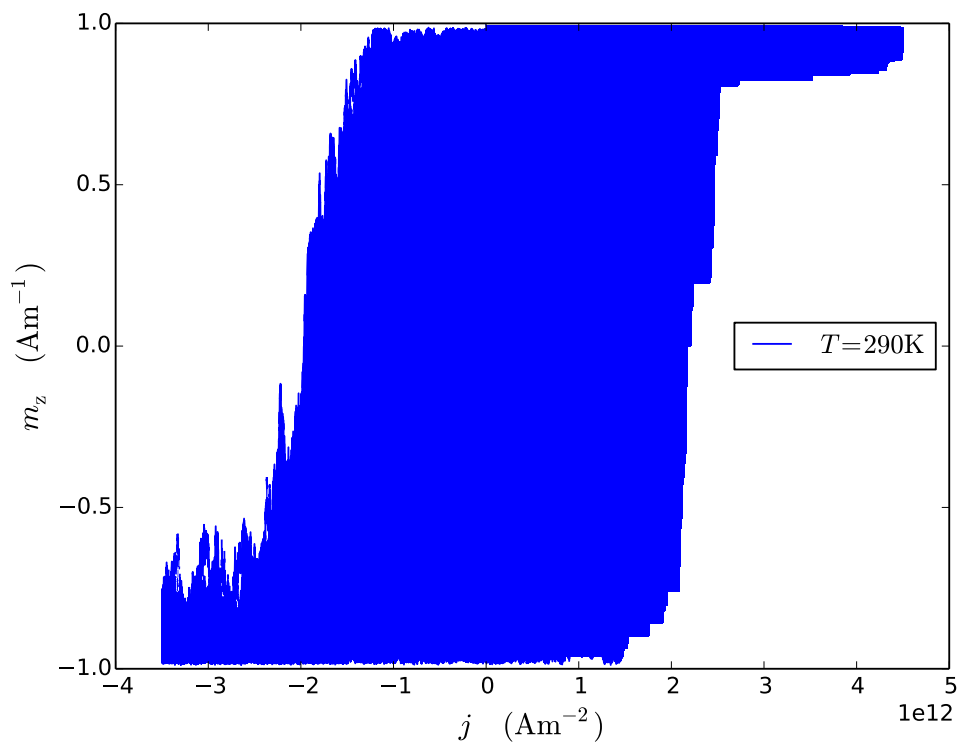


Figure 15: Result of 25 hysteresis cycles at room temperature  $T = 290\text{K}$  and  $H_{\text{ext}} = 0\text{Am}^{-1}$ .

ing thermal fluctuations more freedom to influence the magnetization, which then leads to a higher coefficient of variation  $c_{\text{ap}}$  due to some thermally, strongly deviated switching currents. The opposite is expected when switching from  $p \rightarrow ap$ , since the higher switching currents now dominate over the effect of thermal fluctuations and therefore lead to a narrower deviation range around the mean. However, even though this simulation does not take an adaptation of the simulation temperature in accordance with energy barrier considerations into account, it shows an interesting result. The means for the switching currents in Fig. 15 are  $\mu = -1.3 \times 10^{12} \text{ Am}^{-2}$  for switching from an antiparallel state to a parallel state and  $\mu = 1 \times 10^{12} \text{ Am}^{-2}$  for switching from parallel to antiparallel, which contradicts the spin-diffusion prediction of deterministic experiments, which say, that switching from a parallel state to an antiparallel one requires higher currents.

In order to improve the previous result, the actual rescaling of the sensor's radius by a factor of  $\alpha' = 10$  has to be taken into account. This leads to a thermally unstable sensor at room temperature, due to its one-dimensional character. Following equation (3.46) for an effective field  $H = 0$ , rearranging it to get an expression for the temperature and taking advantage of the sensor's cylindrical shape, leads to the following relations

$$\begin{aligned} T &= \frac{K_{\text{uni}}V}{70k_{\text{B}}} \\ V &= r_{\text{s}}^2\pi z \\ r_{\text{s}} &= \frac{r}{\alpha'} \quad , \end{aligned} \tag{4.6}$$

with  $T$  being the temperature,  $K_{\text{uni}} = 2 \times 10^5 \text{ J/m}^3$  and  $k_{\text{B}}$  standing for the uniaxial anisotropy constant of the free layer and the Boltzmann's constant, and  $r = 30 \text{ nm}$ ,  $r_{\text{s}} = 3 \text{ nm}$  and  $z = 3 \text{ nm}$  representing the free layer's radius, the rescaled radius and height, respectively. The resulting temperature with a ratio of  $K_{\text{uni}}V/k_{\text{B}}T' = 70$  acts as an upper limit  $T'$ , for which the system is considered to be sufficiently stable. In order to avoid critical behaviour of the sensor's polarizer at said boundary temperature  $T'$ , the simulation temperature  $T_{\text{s}}$  is chosen to be  $T_{\text{s}} = 6.88 \text{ K}$  which equals 39% of  $T'$ . The Gilbert damping is set to  $\alpha = 0.2$  and the simulation time is chosen to be  $t_{\text{sim}} = 2 \text{ ns}$  with a constant step size of  $\delta t = 1 \times 10^{-5} \text{ ns}$ . Figure 16 shows a summary of the conducted numerical experiments. Each data point in this plot represents an averaged value of the switching current  $j_{\text{s}}$ , with its corresponding standard deviation  $\sigma_{\text{j}}$ , calculated at different external fields, that are given in normalized values with respect to the anisotropy field. In order to get a satisfying sample size, while at the same time keeping the necessary simulation times reasonably small, a number of 128 hysteresis cycles per point is cho-

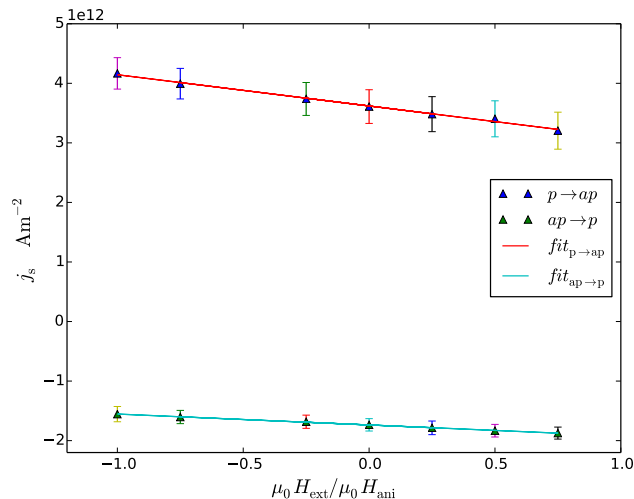


Figure 16: Averaged switching currents at different external fields. Top data points correspond to switching from parallel to antiparallel (higher absolute values of currents) while the bottom data points correspond to switching from antiparallel to parallel (lower absolute values of currents). Standard deviations for each average are indicated with error bars, and a linear function is fitted to each set of data.

sen. Using a linear function, as given in Eq. (4.2), to fit these data, the sensor's gain calculates to  $a_{p \rightarrow ap} = (-5.2 \pm 0.2) \times 10^{11}$  Am $^{-2}$  and  $a_{ap \rightarrow p} = (-1.8 \pm 0.3) \times 10^{11}$  Am $^{-2}$ . The results for the zero offsets are  $b_{p \rightarrow ap} = (3.62 \pm 0.01) \times 10^{12}$  Am $^{-2}$  and  $b_{ap \rightarrow p} = (-1.737 \pm 0.002) \times 10^{12}$  Am $^{-2}$ . It is important to note, that in comparison to the results of the simulations at room temperature, which have the same antiparallel starting configuration for the magnetic layers, the simulations using the rescaled temperature, see Fig. 16, now show higher switching currents and standard deviations when switching from a parallel to an antiparallel state once again.

In order to support the claim, that a linear sensor gain can be deduced from the data presented in Fig. 16, a Fast Fourier Transformation (FFT) of the output signal is performed. An extract of the used rectangular output function at  $\mu_0 H_{\text{ext}} / \mu_0 H_{\text{ani}} = -1.0$  is given in Fig. 17 (a). Figure 17 (b) shows the magnitudes of the 2<sup>nd</sup> harmonics of the FFT at different magnetic fields (blue dots). By fitting these data, a linear correlation (orange line) between the magnetic field and the 2<sup>nd</sup> harmonic of the FFT is confirmed. This confirmation is somewhat weak though, due to the small number of simulated hysteresis cycles per field (128 cycles).

In order to calculate the detectivities  $D$ , an average of the standard deviations  $\sigma_j$  has

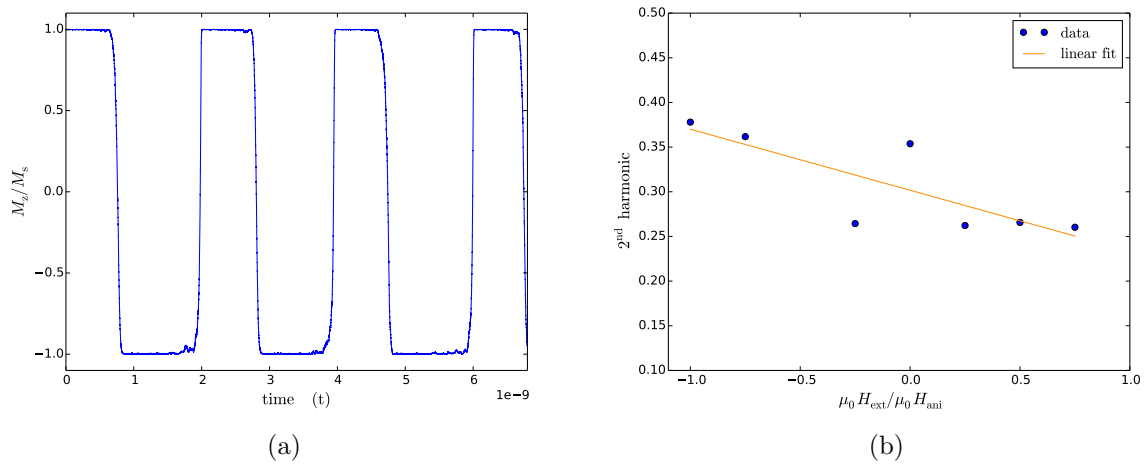


Figure 17: Figure (a) shows an excerpt of the output signal obtained at  $\mu_0 H_{\text{ext}}/\mu_0 H_{\text{ani}} = -1.0$  and Fig. (b) shows magnitudes of the 2<sup>nd</sup> harmonics of the FFT (blue dots) and their linear fit function (orange line).

	$S$	$D$
ap $\rightarrow$ p	$(-1.8 \pm 0.3) \times 10^{11} \text{ Am}^{-2}$	$19 \mu\text{T}/\sqrt{\text{Hz}}$
p $\rightarrow$ ap	$(-5.2 \pm 0.2) \times 10^{11} \text{ Am}^{-2}$	$17 \mu\text{T}/\sqrt{\text{Hz}}$

Table 4: Sensitivities  $S$  and detectivities  $D$  after 128 hysteresis cycles for a measurement time of  $t = 2 \text{ ns}$  for both flanks of the sensor's hysteresis curve, i.e. ap  $\rightarrow$  p and p  $\rightarrow$  ap.

to be computed, since  $\sigma_j$  varies for different fields within a 16% and 15% range, for switching processes from p  $\rightarrow$  ap and ap  $\rightarrow$  p, respectively. With these averaged standard deviations of  $\sigma_{j,p \rightarrow \text{ap}} = 2.8 \times 10^{11} \text{ Am}^{-2}$  and  $\sigma_{j,\text{ap} \rightarrow \text{p}} = 1.1 \times 10^{11} \text{ Am}^{-2}$  and the help of Eq. (2.7), the detectivities can be calculated to  $D_{p \rightarrow \text{ap}} = 17 \mu\text{T}/\sqrt{\text{Hz}}$  and  $D_{\text{ap} \rightarrow \text{p}} = 19 \mu\text{T}/\sqrt{\text{Hz}}$ . Table 4 contains a summary of the results obtained from the stochastic simulations.

## 5 Conclusion

The first aim of this thesis was to design a sensor model, that is sensitive to the z-component of an external magnetic field  $H_{\text{ext}} = H_z$ . With that task accomplished, the next steps included the determination of the sensor's transfer characteristic as well as the discovery of means to lower the required current densities and investigations of the influence, that thermal fluctuations of the magnetization configuration have on the sensor's operation.

The proposed sensor design is based upon a multilayer structure of ferromagnetic and nonmagnetic layers that allow the use of the GMR, in order to get an output signal, that resembles the sensor's state of resistance. The very structure permits the generation of a spin polarized current, that is responsible for the actual switching between the low- and high-resistance states, via spin-torque exertion. Thanks to the use of materials with a perpendicular magnetic anisotropy (PMA), the sensor is designed to be sensitive to the magnetic field component along that distinct direction. Deterministic simulations showed, that a linear correlation between the measured fields and the switching currents  $j_s$  exist. The sensitivity  $S$ , i.e. the slope of that linear function, was found to be larger when switching from a parallel to an antiparallel configuration.

In order to find means of lowering the switching currents, the idea of simply enlarging the free layer, while at the same time reducing its uniaxial anisotropy, was pursued. Simulations, in which the free layer's size was changed within several nm, clearly showed a reduction of the switching currents at both flanks of the hysteresis curve. Another interesting finding was, that currents with a higher degree of polarization were able to switch a smaller free layer earlier than a larger one when switching from  $ap \rightarrow p$ , while currents with a lower degree of polarization were able to induce magnetic reversal more easily within a larger layer when switching from  $p \rightarrow ap$ .

Analysis of the stochastic simulations yielded the expected result, that thermal fluctuations in the magnetic layers have a destabilizing effect and thus also aid the task of lowering the required switching currents. Comparison of the switching currents, calculated in deterministic simulations and stochastic simulations for the same magnetic field show a reductions of  $j_s$  of roughly one magnitude, while switching is supported by thermal fluctuations. The linear relation between switching currents and the magnetic field was confirmed and standard deviations of the simulated data points were within a reasonable range. Furthermore, a Fourier analysis of the rectangular output signal also yielded a linear correlation between the magnitude of the 2<sup>nd</sup> harmonic and the magnetic

field, thus giving another hint to the viability of the sensor. Also, calculations of the sensor's detectivities  $D_{\text{ap} \rightarrow \text{p}} = 19 \mu\text{T}/\sqrt{\text{Hz}}$  and  $D_{\text{p} \rightarrow \text{ap}} = 17 \mu\text{T}/\sqrt{\text{Hz}}$  yielded reasonable results.

Over the course of this thesis, several interesting future tasks arose. The influence of the free layer's size on the switching currents is one of them, since there seems to exist a sweet spot, for which switching currents for both directions benefit the most. Connected to that topic, the investigation of the addition of a second spin polarizer on top of the free layer should be promising. This could lead to a drastic reduction of the required switching currents in both directions. Though, in order to preserve the asymmetric shift of the hysteresis curve due to spin-torque effects, the use of polarizers of different strengths is crucial.

Since thermal fluctuations have been treated at just a single temperature in this thesis, further studies at different temperatures should be conducted to learn more about the sensor's behaviour. Taking this one step further, it would mean to also consider the so far neglected, inner structure of the fixed layer and find means to make its magnetization configuration more resilient against destabilizing effects, such as thermal fluctuations, back scattered electrons and demagnetization fields of the other ferromagnetic layers.

---

## References

- [1] M. N. Baibich and J. M. Broto and A. Fert and F. Nguyen Van Dau and F. Petroff, "Giant Magnetoresistance of (001)Fe/(001)Cr Magnetic Superlattices," *Physical Review Letters*, vol. 61, no. 21, 1988.
- [2] G. Binasch, P. Grunberg, F. Saurenbach, W. Zinn, "Enhanced magnetoresistance in layered magnetic structures with antiferromagnetic interlayer exchange," *Physical Review B*, vol. 39, no. 7, 1989.
- [3] C.-G. Stefanita, *Magnetism*. Springer, 2012.
- [4] A. Tsoukatos, S. Gupta, Y. Huai, "Room Temperature GMR Studies in (Cr, Ta)/[Au/NiFe]<sub>n</sub> Multilayers," *IEEE Transactions on Magnetics*, vol. 33, no. 5, 1997.
- [5] J. Slonczewski, "Currents and torques in metallic magnetic multilayers," *Journal of Magnetism and Magnetic Materials*, vol. 247, no. 324-338, 2002.
- [6] L. Breth, *Detection of weak magnetic fields: The TMR fluxgate sensing technology and its limits*. PhD thesis, Technische Universität Wien, 2016.
- [7] S. Tumanski, *Handbook of Magnetic Measurements*. CRC Press, 2016.
- [8] A.J. Shapiro, V.S. Gornakov, V.I. Nikitenko, R.D. McMichael, W.F. Egelhoff, Y.W. Tahk, R.D. Shull, Li Gan, "Features of domain nucleation and growth in co/ru/co synthetic antiferromagnets deposited on obliquely sputtered ta underlayers," *Journal of Magnetism and Magnetic Materials*, vol. 240, no. 1-3, 2002.
- [9] R. Skomski, *Simple Models of Magnetism*. Oxford University Press, 2008.
- [10] L. Landau, E. Lifshitz, "On the theory of the dispersion of magnetic permeability in ferromagnetic bodies," *Phys. Z. Sowjetunion*, vol. 8, 1935.
- [11] M. L. Bellac, *Quantum Physics*. Cambridge University Press, 2006.
- [12] T. L. Gilbert, "A phenomenological theory of damping in ferromagnetic materials," *IEEE Transactions on Magnetics*, vol. 40, no. 6, 2004.
- [13] D. J. Craik, "Cobalt-platinum permanent magnets," *Platinum Metals Rev.*, vol. 16, no. 4, 1972.

- 
- [14] J. M. D. Coey, *Magnetism and Magnetic Materials*. Cambridge University Press, 2010.
- [15] E.C. Stoner, F.R.S. and E. P. Wolfarth, “A mechanism of magnetic hysteresis in heterogeneous alloys,” *IEEE Transactions on Magnetism*, vol. 27, no. 4, 1991.
- [16] P. Dirac, “On the theory of quantum mechanics,” *Proceedings of the Royal Society A*, vol. 112, no. 762, 1926.
- [17] W. Heisenberg, “Mehrkörperproblem und Resonanz in der Quantenmechanik,” *Zeitschrift für Physik*, vol. 38, no. 6-7, 1926.
- [18] G. Hilscher, *Festkörperphysik I, Teil 2: Magnetismus und Supraleitung*. 2010.
- [19] C. Abert, “Cell-Size Independent Micromagnetic Simulations Including Temperature,” Master’s thesis, Universität Hamburg, 2010.
- [20] W. Scholz, “Micromagnetic simulation of thermally activated switching in fine particles,” Master’s thesis, Technische Universität Wien, 1999.
- [21] J. Slonczewski, “Current-driven excitation of magnetic multilayers,” *Journal of Magnetism and Magnetic Materials*, vol. 159, no. 1-2, 1996.
- [22] S. Zhang and Z. Li, “Roles of nonequilibrium conduction electrons on the magnetization dynamics of ferromagnets,” *Physical Review Letters*, vol. 93, no. 12, 2004.
- [23] Claas Abert, Michele Ruggeri, Florian Bruckner, Christoph Vogler, Aurelien Manchon, Dirk Praetorius and Dieter Suess, “A three-dimensional spin-diffusion model for micromagnetics,” *Scientific Reports*, vol. 5, 2015.
- [24] Claas Abert, Michele Ruggeri, Florian Bruckner, Christoph Vogler, Aurelien Manchon, Dirk Praetorius and Dieter Suess, “A self-consistent spin-diffusion model for micromagnetics,” *Scientific Reports*, vol. 6, 2016.
- [25] W. Wernsdorfer, E. Bonet Orozco, K. Hasselbach, A. Benoit, B. Barbara, N. Demony, A. Loiseau, H. Pascard, and D. Mailly, “Experimental Evidence of the Néel-Brown Model of Magnetization Reversal,” *Physical Review Letters*, vol. 78, no. 9, 1997.
- [26] D. Suess, T. Schrefl, S. Fähler, M. Kirschner, G. Hrkac, F. Dorfbauer, and J. Fidler, “Exchange spring media for perpendicular recording,” *Applied Physics Letters*, vol. 87, no. 1, 2005.
-

- [27] Shoji Ikeda, Jun Hayakawa, Young Min Lee, Fumihiro Matsukura, Yuzo Ohno, Takahiro Hanyu, and Hideo Ohno, “Magnetic tunnel junctions for spintronic memories and beyond,” *IEEE Transactions on Electron Devices*, vol. 54, no. 5, 2007.
- [28] B. Holzmann, “Simulation and Design of a z-Field Sensitive GMR-Sensor.” Technische Universität Wien, 2016.
- [29] C. Abert, *magnum.fe Documentation*, vol. 1.2.0. 2016.